

# Mesoscale Molecular Simulations of Fabry–Pérot Vibrational Strong Coupling

Tao E. Li<sup>a)</sup>

*Department of Physics and Astronomy, University of Delaware, Newark, Delaware 19716, USA*

Developing theoretical frameworks for vibrational strong coupling (VSC) beyond the single-mode approximation is crucial for a comprehensive understanding of experiments with planar Fabry–Pérot cavities. Herein, a generalized cavity molecular dynamics (CavMD) scheme is developed to simulate VSC of a large ensemble of realistic molecules coupled to an arbitrary 1D or 2D photonic environment. This approach is built upon the Power–Zienau–Woolley Hamiltonian in the normal mode basis and uses a grid representation of the molecular ensembles to reduce the computational cost. When simulating the polariton dispersion relation for a homogeneous distribution of molecules in planar Fabry–Pérot cavities, our data highlight the importance of preserving the in-plane translational symmetry of the molecular distribution. In this homogeneous limit, CavMD yields the consistent polariton dispersion relation as analytic theory, i.e., incorporating many cavity modes with varying in-plane wave vectors ( $k_{\parallel}$ ) produces the same spectrum as the system with a single cavity mode. Furthermore, CavMD reveals that the validity of the single mode approximation is challenged when nonequilibrium polariton dynamics are considered, as polariton-polariton scattering occurs between modes with nearest neighbor  $k_{\parallel}$ . Looking forward, our generalized CavMD approach may facilitate understanding vibrational polariton transport and condensation.

## I. INTRODUCTION

Vibrational strong coupling (VSC) has recently attracted great attention due to its potential for modifying molecular properties with vacuum electromagnetic fields.<sup>1–9</sup> Most VSC experiments to date have been performed in planar Fabry–Pérot cavities, in which the Rabi splitting between an infrared (IR) cavity mode and a vibrational mode of a large collection of molecules is observed in the linear IR spectrum.<sup>10–15</sup> Alongside the exciting yet sometimes controversial experimental observations,<sup>16–18</sup> theoretical work on VSC<sup>19–33</sup> usually builds upon different levels of approximations; the most pervasive approximation being that only a single or a few cavity modes are taken into account. However, as will be discussed in detail in this work, because planar Fabry–Pérot cavities contain a continuum of cavity modes along the cavity mirror plane,<sup>11</sup> the single-mode approximation might break down.

For example, under electronic strong coupling, experimentally observed exciton-polariton condensates originate from elastic scattering between lower polaritons at different in-plane wave vectors (as denoted by  $k_{\parallel}$ ).<sup>34,35</sup> In other words, including cavity modes at different  $k_{\parallel}$  values is necessary for a proper description of exciton-polariton condensates. As another example, Ebbesen and coworkers observed that VSC catalytic effects occur only when the cavity mode at  $k_{\parallel} = 0$  is at resonance with a vibrational mode of molecules.<sup>3,5</sup> These examples make it clear that the single-mode approximation is insufficient for describing these strong coupling effects in Fabry–Pérot cavities, and the full cavity dispersion relation must be considered.

Some recent studies have employed numerical simulations to investigate electronic strong coupling in multi-mode one-dimensional (1D) Fabry–Pérot cavities.<sup>36–39</sup> Under VSC conditions, however, most theoretical approaches have relied on the single-mode approximation, with an explicit treatment of the multi-mode Fabry–Pérot cavities discussed only for model systems.<sup>40,41</sup> It is thus necessary to extend theoretical approaches for VSC, including electronic structure theory and molecular dynamics simulations, to the multi-mode case. Moreover, only by developing an adequate theoretical description of the multi-mode cavities, one can examine whether conclusions made in the single-mode limit still hold for more realistic cavity setups.

One efficient simulation tool for describing VSC in the single-mode limit is the cavity molecular dynamics (CavMD) approach,<sup>33</sup> in which the dynamics of a large ensemble of molecules coupled to a single cavity mode (or a few cavity modes) are propagated classically or semiclassically (via path integrals) on the electronic ground state surface. Some notable results of CavMD are worth mentioning. (i) Under thermal equilibrium, properties of individual molecules remain invariant inside versus outside the cavity even when nuclear and photonic quantum effects are considered.<sup>33,42</sup> (ii) In the linear response limit, the polariton spectrum described by CavMD is equivalent to that described by coupled oscillator models.<sup>33,43</sup> (iii) In the weak excitation limit, the relaxation rates of the upper polariton (UP) have the same parameter dependence as the Fermi’s golden rule rate of a tight-binding harmonic model.<sup>44</sup> (iv) In strong pumping regime, CavMD predicts novel mechanisms, including lower-polariton (LP) enhanced molecular nonlinear absorption,<sup>45</sup> a behavior that has been observed experimentally,<sup>46</sup> as well as strong energy accumulation in solute molecules by exciting the solvent

<sup>a)</sup>Electronic mail: taoli@udel.edu

LP.<sup>47</sup> The CavMD approach has also recently embraced a quantum mechanical/molecular mechanical (QM/MM) description of the molecular systems. This advance enables the direct simulation of ultrafast VSC experiments such as the pseudorotation “reaction” of the Fe(CO)<sub>5</sub> solute in the *n*-dodecane solvent,<sup>48</sup> although more extensive simulations (i.e., by including a large number of replicas of the solute-solvent molecular systems) are needed to understand the mechanisms of the ultrafast experiments.

In this manuscript, we extend the CavMD approach to describe VSC in arbitrary cavity setups, especially Fabry–Pérot cavities with  $k_{\parallel}$ -dependent cavity modes. We perform numerical experiments to highlight the importance of the in-plane translational symmetry in reproducing the  $k_{\parallel}$ -dependent polariton branches observed in experiments. Additionally, utilizing nonequilibrium CavMD simulations, we provide initial data on polariton-polariton scattering with neighboring  $k_{\parallel}$  values, a fundamental mechanism which is relevant to the formation of polariton condensates. Finally, our numerical experiments suggests research opportunities of preparing VSC in the absence of the molecular in-plane translational symmetry.

The manuscript is organized as follows. In Sec. II, we present a derivation of CavMD in arbitrary photonic environments, especially in Fabry–Pérot-like cavities. Sec. III provides simulation details. In Sec. IV, we present CavMD results for a few cavity setups. In Sec. V, we discuss the importance of the in-plane translational symmetry. We conclude in Sec. VI.

## II. THEORY

### A. QED Hamiltonian in a photonic structure

We start with the Power–Zienau–Woolley Hamiltonian for light-matter interactions:<sup>49</sup>

$$\hat{H}_{\text{QED}} = \hat{H}_{\text{M}} + \hat{H}_{\text{ph}} + \hat{H}_{\text{int}}. \quad (1)$$

Here,  $\hat{H}_{\text{M}}$  denotes the standard molecular (kinetic + potential) Hamiltonian;  $\hat{H}_{\text{ph}}$  denotes the photonic Hamiltonian:

$$\hat{H}_{\text{ph}} = \frac{1}{2} \int d\mathbf{r} \left( \frac{1}{\varepsilon_0} |\hat{\mathbf{D}}_{\perp}(\mathbf{r})|^2 + \frac{1}{\mu_0} |\hat{\mathbf{B}}(\mathbf{r})|^2 \right), \quad (2)$$

where  $\hat{\mathbf{D}}_{\perp}(\mathbf{r})$  and  $\hat{\mathbf{B}}(\mathbf{r})$  are the displacement and magnetic field operators, and  $\varepsilon_0$  and  $\mu_0$  denote the vacuum permittivity and permeability, respectively;  $\hat{H}_{\text{int}}$  denotes the Hamiltonian that governs the light-matter interaction:

$$\hat{H}_{\text{int}} = -\frac{1}{\varepsilon_0} \int d\mathbf{r} \hat{\mathbf{D}}_{\perp}(\mathbf{r}) \cdot \hat{\mathcal{P}}_{\perp}(\mathbf{r}) + \frac{1}{2\varepsilon_0} \int d\mathbf{r} |\hat{\mathcal{P}}_{\perp}(\mathbf{r})|^2. \quad (3)$$

Here, the transverse polarization density operator  $\hat{\mathcal{P}}_{\perp}(\mathbf{r})$  is defined as<sup>49</sup>

$$\hat{\mathcal{P}}_{\perp}(\mathbf{r}) = \int d\mathbf{r}' \overleftrightarrow{\delta}_{\perp}(\mathbf{r} - \mathbf{r}') \hat{\mathcal{P}}(\mathbf{r}'), \quad (4)$$

where the polarization density operator  $\hat{\mathcal{P}}(\mathbf{r})$  reads

$$\hat{\mathcal{P}}(\mathbf{r}) = \sum_i Q_i \hat{\mathbf{r}}_i \delta(\mathbf{r} - \mathbf{r}_i). \quad (5)$$

In Eq. (5),  $Q_i$  denotes the charge of the  $i$ -th particle, which can be either an electron or a nucleus;  $\hat{\mathbf{r}}_i$  denotes the position operator of the particle. In Eq. (4), the transverse  $\delta$ -function  $\overleftrightarrow{\delta}_{\perp}(\mathbf{r} - \mathbf{r}')$  is a rank-two tensor:

$$\overleftrightarrow{\delta}_{\perp}(\mathbf{r} - \mathbf{r}') = \sum_{k\lambda} \mathbf{f}_{k\lambda}(\mathbf{r}) \mathbf{f}_{k\lambda}^*(\mathbf{r}'). \quad (6)$$

Here,  $\mathbf{f}_{k\lambda}(\mathbf{r})$  denotes the mode function of the photon with wave vector  $k \equiv |\mathbf{k}|$  and two possible polarization directions indexed by  $\lambda$ , and  $\mathbf{f}_{k\lambda}^*(\mathbf{r})$  denotes its complex conjugate. The explicit form of  $\mathbf{f}_{k\lambda}(\mathbf{r})$  depends on the boundary conditions of the dielectric medium; it can be obtained by solving the Helmholtz equation  $\nabla \times \nabla \times \mathbf{f}_{k\lambda} - k^2 \mathbf{f}_{k\lambda} = 0$ . For example, in vacuum,  $\mathbf{f}_{k\lambda}(\mathbf{r}) = \boldsymbol{\xi}_{\lambda} e^{i\mathbf{k} \cdot \mathbf{r}} / \sqrt{\Omega}$ , where  $\boldsymbol{\xi}_{\lambda}$  denotes the unit vector along the photon polarization direction, and  $\Omega$  denotes the quantization volume.

### 1. Normal mode representation

The field operators in Eqs. (2) and (3) can also be represented in the normal mode representation. In the normal mode representation, the displacement field operator  $\hat{\mathbf{D}}_{\perp}(\mathbf{r})$  reads

$$\hat{\mathbf{D}}_{\perp}(\mathbf{r}) = \hat{\mathbf{D}}(\mathbf{r}) = \sum_{k\lambda} iD_k \left[ \hat{a}_{k\lambda} \mathbf{f}_{k\lambda}(\mathbf{r}) - \hat{a}_{k\lambda}^{\dagger} \mathbf{f}_{k\lambda}^*(\mathbf{r}) \right]. \quad (7)$$

Here,  $D_k = \sqrt{\hbar\omega_k \varepsilon_0 / 2}$ , where  $\omega_k$  denotes the photonic frequency, and  $\hat{a}_{k\lambda}^{\dagger}$  ( $\hat{a}_{k\lambda}$ ) denotes the creation (annihilation) operator of the photon mode. In Eq. (2), the magnetic field operator is given by  $\hat{\mathbf{B}}(\mathbf{r}) = \frac{1}{\sqrt{\varepsilon_0}} \nabla \times \hat{\mathbf{A}}(\mathbf{r})$ . Here, the vector potential  $\hat{\mathbf{A}}(\mathbf{r})$  is

$$\hat{\mathbf{A}}_{\perp}(\mathbf{r}) = \sum_{k\lambda} A_k \left[ \hat{a}_{k\lambda} \mathbf{f}_{k\lambda}(\mathbf{r}) + \hat{a}_{k\lambda}^{\dagger} \mathbf{f}_{k\lambda}^*(\mathbf{r}) \right], \quad (8)$$

where  $A_k = \sqrt{\hbar/2\omega_k \varepsilon_0}$ . Hence, in the normal mode representation, the photonic Hamiltonian in Eq. (2) can be expressed as

$$\hat{H}_{\text{ph}} = \sum_{k\lambda} \hbar\omega_k \hat{a}_{k\lambda}^{\dagger} \hat{a}_{k\lambda}. \quad (9)$$

Given a collection of  $N$  charge-neutral molecules, let  $\hat{\boldsymbol{\mu}}^{(n)}$  be the molecular dipole operator of the  $n$ -th molecule. The polarization density operator  $\hat{\mathcal{P}}(\mathbf{r})$  in Eq. (5) can be rewritten as

$$\hat{\mathcal{P}}(\mathbf{r}) = \sum_{n=1}^N \hat{\boldsymbol{\mu}}^{(n)} \delta(\mathbf{r} - \mathbf{r}_n), \quad (10)$$

where  $\mathbf{r}_n$  denotes the position of the  $n$ -th molecule. When Eq. (10) is substituted into the light-matter interaction Hamiltonian defined in Eq. (3),  $\hat{H}_{\text{int}}$  becomes<sup>50</sup>

$$\begin{aligned} \hat{H}_{\text{int}} = & - \sum_{k\lambda} \sum_{n=1}^N iD_k \left[ \hat{a}_{k\lambda} \mathbf{f}_{k\lambda}(\mathbf{r}_n) - \hat{a}_{k\lambda}^\dagger \mathbf{f}_{k\lambda}^*(\mathbf{r}_n) \right] \cdot \hat{\boldsymbol{\mu}}^{(n)} \\ & + \sum_{k\lambda} \frac{1}{2\epsilon_0} \left| \sum_{n=1}^N \hat{\boldsymbol{\mu}}^{(n)} \cdot \mathbf{f}_{k\lambda}(\mathbf{r}_n) \right|^2. \end{aligned} \quad (11)$$

To proceed, we further rewrite  $\hat{a}_{k\lambda}$  and  $\hat{a}_{k\lambda}^\dagger$  as  $\hat{p}_{k\lambda}$  and  $\hat{q}_{k\lambda}$ :

$$\hat{a}_{k\lambda} = \frac{1}{\sqrt{2\hbar\omega_k}} (\omega_k \hat{q}_{k\lambda} + i\hat{p}_{k\lambda}), \quad (12a)$$

$$\hat{a}_{k\lambda}^\dagger = \frac{1}{\sqrt{2\hbar\omega_k}} (\omega_k \hat{q}_{k\lambda} - i\hat{p}_{k\lambda}). \quad (12b)$$

When Eq. (12) is substituted into  $\hat{H}_{\text{ph}}$  in Eq. (9) as well as  $\hat{H}_{\text{int}}$  in Eq. (11), the field-related Hamiltonian  $\hat{H}_{\text{F}} \equiv \hat{H}_{\text{ph}} + \hat{H}_{\text{int}}$  can be expressed as:

$$\begin{aligned} \hat{H}_{\text{F}} = & \sum_{k\lambda} \frac{1}{2} \omega_k^2 \left( \hat{q}_{k\lambda} - \sum_{n=1}^N \frac{\hat{\boldsymbol{\mu}}^{(n)}}{\sqrt{\epsilon_0 \omega_k}} \cdot \text{Im}[\mathbf{f}_{k\lambda}(\mathbf{r}_n)] \right)^2 \\ & + \frac{1}{2} \left( \hat{p}_{k\lambda} - \sum_{n=1}^N \frac{\hat{\boldsymbol{\mu}}^{(n)}}{\sqrt{\epsilon_0}} \cdot \text{Re}[\mathbf{f}_{k\lambda}(\mathbf{r}_n)] \right)^2. \end{aligned} \quad (13)$$

At this point, we assume that  $\mathbf{f}_{k\lambda}(\mathbf{r}_n)$  is always real-valued, so  $\text{Im}[\mathbf{f}_k(\mathbf{r}_n)] \equiv 0$  and only  $\hat{p}_{k\lambda}$  is coupled to the molecules. Because photons are harmonic oscillators, it is also trivial to exchange  $\hat{p}_{k\lambda}$  and  $\hat{q}_{k\lambda}$  in Eq. (13), which leads to:

$$\hat{H}_{\text{F}} = \sum_{k\lambda} \frac{1}{2} \hat{p}_{k\lambda}^2 + \frac{1}{2} \omega_k^2 \left( \hat{q}_{k\lambda} + \sum_{n=1}^N \frac{\hat{\boldsymbol{\mu}}^{(n)} \cdot \mathbf{f}_{k\lambda}(\mathbf{r}_n)}{\sqrt{\epsilon_0 \omega_k}} \right)^2. \quad (14)$$

Eq. (14) can be regarded as a generalized, multi-mode form of the widely used single-mode Pauli-Fierz Hamiltonian.

## 2. Toward molecular dynamics simulations

To be suitable for molecular dynamics simulations, the quantum position and momentum operators of photons are rescaled as

$$\hat{p}_{k\lambda} = \tilde{\hat{p}}_{k\lambda} / \sqrt{m_{k\lambda}}, \quad (15a)$$

$$\hat{q}_{k\lambda} = \tilde{\hat{q}}_{k\lambda} \sqrt{m_{k\lambda}}, \quad (15b)$$

where  $m_{k\lambda}$  denotes the auxiliary mass of the photon mode, which is introduced to make the photonic dynamics compatible with conventional molecular dynamics

packages. With this rescaling, the field-related Hamiltonian in Eq. (14) becomes

$$\begin{aligned} \hat{H}_{\text{F}} = & \sum_{k\lambda} \frac{1}{2m_{k\lambda}} \tilde{\hat{p}}_{k\lambda}^2 \\ & + \frac{1}{2} m_{k\lambda} \omega_k^2 \left( \tilde{\hat{q}}_{k\lambda} + \sum_{n=1}^N \frac{\hat{\boldsymbol{\mu}}^{(n)} \cdot \mathbf{f}_{k\lambda}(\mathbf{r}_n)}{\sqrt{\epsilon_0 m_{k\lambda} \omega_k}} \right)^2. \end{aligned} \quad (16)$$

Finally, we project the QED Hamiltonian in Eq. (16) to the electronic ground state. Under this cavity Born-Oppenheimer approximation,<sup>51</sup> the light-matter Hamiltonian becomes

$$\hat{H}_{\text{QED}}^{\text{G}} = \hat{H}_{\text{M}}^{\text{G}} + \hat{H}_{\text{F}}^{\text{G}}, \quad (17a)$$

where  $\hat{H}_{\text{M}}^{\text{G}}$  denotes the conventional (kinetic + potential) molecular Hamiltonian in the electronic ground state, and the field-related Hamiltonian becomes

$$\begin{aligned} \hat{H}_{\text{F}}^{\text{G}} = & \sum_{k\lambda} \frac{1}{2m_{k\lambda}} \tilde{\hat{p}}_{k\lambda}^2 \\ & + \frac{1}{2} m_{k\lambda} \omega_k^2 \left( \tilde{\hat{q}}_{k\lambda} + \sum_{n=1}^N \frac{\hat{\boldsymbol{\mu}}_{\text{g}}^{(n)} \cdot \mathbf{f}_{k\lambda}(\mathbf{r}_n)}{\sqrt{\epsilon_0 m_{k\lambda} \omega_k}} \right)^2. \end{aligned} \quad (17b)$$

Here,  $\hat{\boldsymbol{\mu}}_{\text{g}}^{(n)}$  denotes the dipole operator of the  $n$ -th molecule under electronic ground state.

The electronic ground-state light-matter Hamiltonian in Eq. (17) resembles the Hamiltonian in Ref. 33. The only difference is that here the long wave approximation is not used and the spatial dependence of the photonic mode functions is explicitly considered. If the long wave approximation is taken here,  $\mathbf{f}_{k\lambda}(\mathbf{r}_n) \equiv \boldsymbol{\xi}_\lambda / \sqrt{\Omega}$  (i.e., there is no spatial variance in the photonic mode functions), Eq. (17) is reduced to the light-matter Hamiltonian in Ref. 33.

## B. Efficient mesoscale CavMD simulations

After obtaining the generalized light-matter Hamiltonian in Eq. (17), we are interested in deriving an efficient simulation scheme of CavMD.

### 1. A brute-force approach

Given the quantum Hamiltonian in Eq. (17), the classical equations of motion of the coupled light-matter system become

$$M_\alpha \ddot{\mathbf{R}}_\alpha = \mathbf{F}_\alpha^{(0)} + \mathbf{F}_\alpha^{\text{cav}}, \quad (18a)$$

$$m_{k\lambda} \ddot{\tilde{q}}_{k\lambda} = -m_{k\lambda} \omega_k^2 \tilde{q}_{k\lambda} - \varepsilon_{k\lambda} d_{\text{g},k\lambda}. \quad (18b)$$

Here,  $d_{\text{g},k\lambda}$  denotes the total molecular dipole moment projected along the cavity polarization direction:

$$d_{\text{g},k\lambda} \equiv \sum_{n=1}^N \sqrt{V} \boldsymbol{\mu}_{\text{g}}^{(n)} \cdot \mathbf{f}_{k\lambda}(\mathbf{r}_n), \quad (18c)$$

where  $\mathcal{V}$ , in the units of volume, denotes the normalization coefficient of the mode function which satisfies  $\langle \mathcal{V} | \mathbf{f}_{k\lambda}(\mathbf{r})|^2 \rangle = 1$ . This normalization guarantees  $\sqrt{\mathcal{V}} \mathbf{f}_{k\lambda}(\mathbf{r}_n)$  to be dimensionless, so  $d_{g,k\lambda}$  maintains the same units as  $\boldsymbol{\mu}_g^{(n)}$ .  $M_\alpha$  and  $\mathbf{R}_\alpha$  denote the mass and position of the  $\alpha$ -th nucleus,  $\mathbf{F}_\alpha^{(0)}$  denotes the nuclear force acting on the  $\alpha$ -th nucleus without the cavity (i.e., the same force as that in conventional molecular dynamics simulations), and  $\mathbf{F}_\alpha^{\text{cav}}$  denotes the force from the cavity acting on the  $\alpha$ -th nucleus:

$$\mathbf{F}_\alpha^{\text{cav}} = - \sum_{k\lambda} \left( \varepsilon_{k\lambda} \tilde{q}_{k\lambda} + \frac{\varepsilon_{k\lambda}^2}{m_{k\lambda} \omega_k^2} d_{g,k\lambda} \right) \frac{\partial d_{g,k\lambda}}{\partial \mathbf{R}_\alpha}, \quad (19)$$

where the effective light-matter coupling  $\varepsilon_{k\lambda}$  is defined as

$$\varepsilon_{k\lambda} \equiv \sqrt{\frac{m_{k\lambda} \omega_k^2}{\mathcal{V} \varepsilon_0}}. \quad (20)$$

Because the dielectric boundary conditions determine the photonic mode functions, given an explicit form of  $\mathbf{f}_{k\lambda}(\mathbf{r}_n)$ , Eq. (18) allows for direct propagation of the coupled photon-molecular dynamics in the dielectric environment. However, due to the large number of molecules and the infinite number of photonic modes involved in planar Fabry-Pérot cavities, a brute-force propagation of Eq. (18) is unrealistic.

Below, using a rectangular parallelepiped as the photonic boundary conditions, we demonstrate how to efficiently simulate CavMD in the mesoscale with an affordable computational cost.

## 2. Photonic mode functions in a rectangular parallelepiped

For a rectangular parallelepiped shown in Fig. 1, the photonic mode functions are<sup>52</sup>

$$f_{k,x} = \sqrt{\frac{8}{\Omega}} \cos(k_x x) \sin(k_y y) \sin(k_z z), \quad (21a)$$

$$f_{k,y} = \sqrt{\frac{8}{\Omega}} \sin(k_x x) \cos(k_y y) \sin(k_z z), \quad (21b)$$

$$f_{k,z} = \sqrt{\frac{8}{\Omega}} \sin(k_x x) \sin(k_y y) \cos(k_z z). \quad (21c)$$

Here,  $\Omega$  denotes the volume of the rectangular parallelepiped;

$$k_x = \frac{l_x \pi}{L_x}, \quad (22a)$$

$$k_y = \frac{l_y \pi}{L_y}, \quad (22b)$$

$$k_z = \frac{l_z \pi}{L_z}, \quad (22c)$$

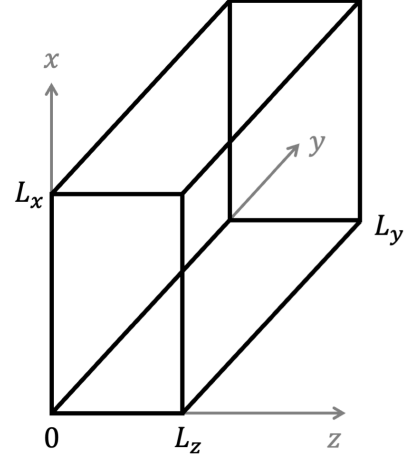


FIG. 1. An optical resonator with volume  $\Omega$  shaped as a rectangular parallelepiped, with lengths along the three dimensions denoted as  $L_x$ ,  $L_y$ , and  $L_z$ . The electric field amplitude is assumed to be zero at the boundaries.

where  $L_x$ ,  $L_y$ , and  $L_z$  denote the lengths of the rectangular parallelepiped in three dimensions, and  $l_x$ ,  $l_y$ , and  $l_z$  are independent integers.

This rectangular parallelepiped can be used to simulate CavMD dynamics in planar Fabry-Pérot cavities. To this end, we assume the cavity is placed along the  $z$  direction and  $L_z \ll L_x, L_y$ . If only the fundamental cavity mode of  $k_z$  is relevant to our research interest (e.g., when the high-frequency vibrational mode of molecules is near resonant with the fundamental cavity mode), we can further take  $k_z = \pi/L_z$  and ignore any higher order modes. If the molecules are placed near the plane of  $z = L_z/2$  (as demonstrated in Fig. 2a), only the following mode functions have a non-zero contribution:

$$f_{k,x} = \sqrt{\frac{8}{\Omega}} \cos(k_x x) \sin(k_y y), \quad (23a)$$

$$f_{k,y} = \sqrt{\frac{8}{\Omega}} \sin(k_x x) \cos(k_y y). \quad (23b)$$

For this cavity setup, the normalization coefficient  $\mathcal{V} = \Omega/2$ , so  $\langle \mathcal{V} | f_{k,x} |^2 \rangle = \langle \mathcal{V} | f_{k,y} |^2 \rangle = 1$ . The corresponding cavity mode frequency  $\omega_k$  becomes

$$\omega_k = c \sqrt{\left( \frac{\pi}{L_z} \right)^2 + k_{\parallel}^2}. \quad (24)$$

Here,  $c = c_0/n_{\text{ref}}$  denotes the speed of light in the medium;  $c_0$  denotes the speed of light in the vacuum and  $n_{\text{ref}}$  denotes the refractive index of the medium. The in-plane wave vector  $k_{\parallel}$  is defined as

$$k_{\parallel}^2 = \left( \frac{l_x \pi}{L_x} \right)^2 + \left( \frac{l_y \pi}{L_y} \right)^2. \quad (25)$$

In practice, we include a finite number of cavity modes with  $1 \leq l_x \leq l_x^{\text{max}}$  and  $1 \leq l_y \leq l_y^{\text{max}}$ .

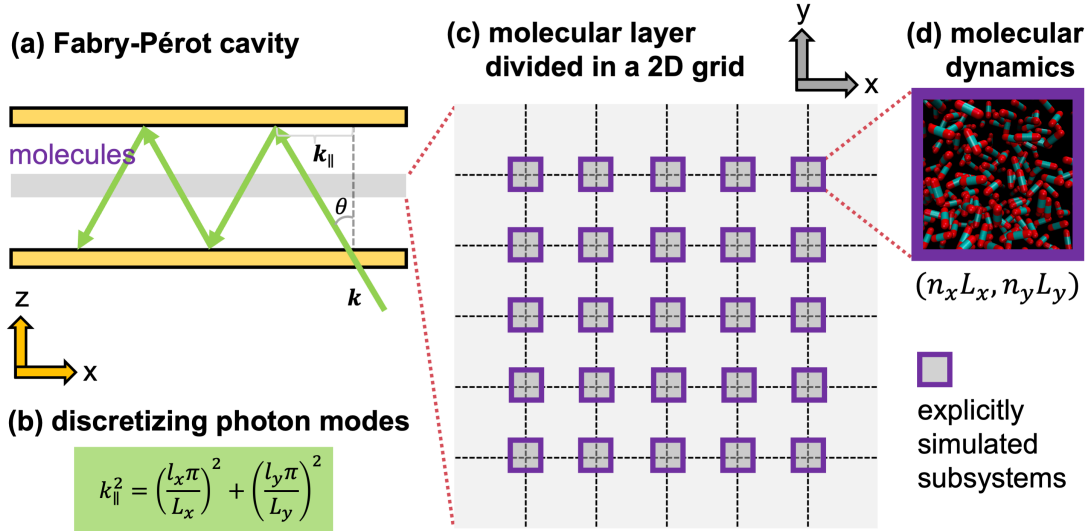


FIG. 2. Strategy for simulating Fabry-Pérot vibrational strong coupling. (a) The Fabry-Pérot cavity viewed in the  $xz$  plane. A layer of molecules is confined at the middle of the cavity. (b) Finite photon modes are simulated by discretizing  $\mathbf{k}_{\parallel}$ . (c) The molecules are divided in a 2D grid along the  $xy$  plane. (d) For an efficient simulation of the macroscopic molecular system, only the small molecular subsystems at different grid points (labeled as the purple squares) are explicitly simulated.

### 3. A 2D grid of molecules

Although we have assumed that the molecules of interest are confined to a thin layer along the plane  $z = L_z/2$  (Fig. 2a), directly simulating all  $N$  molecules in this layer is computationally expensive. Thus, we approximate the full molecular system by a smaller number of model grid points (Fig. 2c), where each grid point represents a finite-sized, explicitly simulated molecular system. This grid representation allows us to simulate the system with much less computational resources.

With the 2D grid representation, the total molecular dipole  $d_{g,k\lambda}$  defined in Eq. (18c) can be calculated as

$$d_{g,k\lambda} = N_{\text{ratio}} d_{g,k\lambda}^{\text{sub}}. \quad (26)$$

Here,  $N_{\text{ratio}}$  denotes the ratio between the true number of molecules in the cavity versus the number of explicitly simulated molecules;  $d_{g,k\lambda}^{\text{sub}}$  denotes the total dipole moment of the explicitly simulated molecules (the purple areas in Fig. 2c),

$$d_{g,k\lambda}^{\text{sub}} = \sum_{\vec{n}=(n_x, n_y)} \sqrt{V} \boldsymbol{\mu}_g^{(\vec{n})} \cdot \mathbf{f}_{k\lambda}(\mathbf{r}_{\vec{n}}), \quad (27)$$

where  $\boldsymbol{\mu}_g^{(\vec{n})}$  denotes the total molecular dipole in each explicitly simulated grid point, and  $\mathbf{r}_{\vec{n}}$  denotes the position of each grid point labeled by  $\vec{n} = (n_x, n_y)$ .

### 4. A practical classical simulation scheme

With the molecular dipole defined above, we can rewrite the equations of motion in Eq. (18) as

$$M_{\alpha} \ddot{\mathbf{R}}_{\alpha} = \mathbf{F}_{\alpha}^{(0)} + \mathbf{F}_{\alpha}^{\text{cav}}, \quad (28a)$$

$$m_{k\lambda} \ddot{q}_{k\lambda} = -m_{k\lambda} \omega_k^2 \tilde{q}_{k\lambda} - \tilde{\varepsilon}_{k\lambda} d_{g,k\lambda}^{\text{sub}}, \quad (28b)$$

where the cavity force is

$$\mathbf{F}_{\alpha}^{\text{cav}} = - \sum_{k\lambda} \left( \tilde{\varepsilon}_{k\lambda} \tilde{q}_{k\lambda} + \frac{\tilde{\varepsilon}_{k\lambda}^2}{m_{k\lambda} \omega_k^2} d_{g,k\lambda}^{\text{sub}} \right) \frac{\partial d_{g,k\lambda}^{\text{sub}}}{\partial \mathbf{R}_{\alpha}}. \quad (28c)$$

Here, we have defined the rescaled photon position  $\tilde{q}_{k\lambda}$  as

$$\tilde{q}_{k\lambda} \equiv \tilde{q}_{k\lambda} / \sqrt{N_{\text{ratio}}} \quad (29)$$

and the new effective light-matter coupling as

$$\tilde{\varepsilon}_{k\lambda} = \sqrt{N_{\text{ratio}}} \varepsilon_{k\lambda} = \sqrt{\frac{N_{\text{ratio}} m_{k\lambda} \omega_k^2}{V \epsilon_0}}. \quad (30)$$

The rescaling introduced in Eqs. (29) and (30) is necessary because it guarantees that the equations of motion in Eq. (28) are of the same form as Eq. (18), except that (i) the total dipole moment of the explicitly simulated molecules  $d_{g,k\lambda}^{\text{sub}}$  replaces the true total dipole moment of the whole molecular layer and (ii)  $\tilde{\varepsilon}_{k\lambda}$  becomes unphysically large. Of course, as demonstrated in previous CavMD work<sup>45,47,53</sup>, because of the potential for artifacts introduced by this rescaling procedure, it is necessary to validate whether the simulated cavity effects can persist

in real experiments containing a macroscopic number of molecules. This validation process can be done by increasing the number of explicitly simulated molecules as well as reducing  $\tilde{\varepsilon}_{k\lambda}$  (these two parameters should be changed in a manner such that the observed Rabi splitting remains the same) until the convergence of the simulation results.

Eq. (28) illustrates that three molecular quantities, i.e.,  $\mathbf{F}_\alpha^{(0)}$ ,  $d_{g,k\lambda}^{\text{sub}}$ , and  $\partial d_{g,k\lambda}^{\text{sub}}/\partial \mathbf{R}_\alpha$ , must be determined during CavMD simulations. Previously, under the single-mode limit, these three quantities have been evaluated using both non-polarizable empirical force fields<sup>33</sup> and hybrid quantum-mechanical molecular-mechanical (QM/MM) calculations<sup>48</sup>.

When non-polarizable force fields are used to describe the molecules, the total dipole moment of the molecular system at each grid point  $\vec{n} = (n_x, n_y)$ , according to Eq. (27), becomes

$$\boldsymbol{\mu}_g^{(\vec{n})} = \sum_{\alpha \in \vec{n}} Q_\alpha \mathbf{R}_\alpha, \quad (31)$$

where  $Q_\alpha$  denotes the partial charge of the  $\alpha$ -th nucleus. Therefore,  $d_{g,k\lambda}^{\text{sub}}$  can be expressed as

$$d_{g,k\lambda}^{\text{sub}} = \sum_{\vec{n}} \sum_{\alpha \in \vec{n}} \sqrt{V} Q_\alpha \mathbf{R}_\alpha \cdot \mathbf{f}_{k\lambda}(\mathbf{r}_{\vec{n}}). \quad (32)$$

Similarly, the dipole derivatives become

$$\frac{\partial d_{g,k\lambda}^{\text{sub}}}{\partial R_{\alpha i}^{(\vec{n})}} = \sqrt{V} Q_\alpha \mathbf{e}_i \cdot \mathbf{f}_{k\lambda}(\mathbf{r}_{\vec{n}}), \quad (33)$$

where  $R_{\alpha i}^{(\vec{n})}$  represents the nuclear position along the  $i$ -th direction at grid point  $\vec{n} = (n_x, n_y)$ , and  $\mathbf{e}_i$  denotes the unit vector along the  $i$ -th direction. When the equations for the dipole and its derivatives [Eqs. (32) and (33)] are substituted into the equations of motion [Eq. (28)], the mesoscale cavity dynamics can be efficiently simulated.

### 5. An outline of mesoscale CavMD simulation

Here, we give a brief outline on how to perform mesoscale CavMD simulations from scratch.

- (i) Determine the cavity mode structure by setting the fundamental cavity frequency  $\omega_\perp = c\pi/L_z$ , cavity mirror plane lengths  $L_x, L_y$ , as well as the maximal mode numbers  $l_x^{\text{max}}, l_y^{\text{max}}$  along the cavity mirror plane [Eqs. (23)-(25)].
- (ii) Determine the number and positions of molecular grid points along the  $(x, y)$  plane, and setup the initial molecular geometry for each grid point [Eqs. (31)-(33)].
- (iii) Given the effective light-matter coupling  $\tilde{\varepsilon}_{k\lambda}$ , run the mesoscale CavMD simulation using Eq. (28).

- (iv) (Optional) Increase the explicitly simulated molecular number  $N_{\text{simu}}$  while reducing the effective coupling strength  $\tilde{\varepsilon}_{k\lambda} \propto 1/\sqrt{N_{\text{simu}}}$  accordingly, then check whether the observed cavity effect is robust for different cavity sizes. The large  $N_{\text{simu}}$  limit should correspond to VSC in realistic planar Fabry-Pérot cavities.

### 6. Connecting to previous CavMD work with a single cavity mode

The present formalism can be reduced to previous CavMD work with only a single cavity mode, which contains two degenerate cavity photons polarized along either the  $x$ - or the  $y$ -direction.<sup>33</sup> This reduction is guaranteed because the equations of motion derived in Eq. (28) are identical to those of our earlier work.<sup>33,45</sup>

In detail, to include only two degenerate cavity photons which are polarized along either the  $x$  or the  $y$  direction, we set  $k_x = \pi/L_x$ ,  $k_y = \pi/L_y$ , and  $L_x = L_y \gg L_z$ . Then, we may use only a single grid point to represent the whole molecular system, where the location of the grid point is denoted  $x = \frac{L_x}{4}$  and  $y = \frac{L_y}{4}$ . With these parameters, both  $k_x x$  and  $k_y y$  equal  $\pi/4$ ; according to Eq. (23), the two possible photon mode functions become

$$f_{k,x} = \sqrt{\frac{2}{\Omega}} = \sqrt{\frac{1}{V}}, \quad (34a)$$

$$f_{k,y} = \sqrt{\frac{2}{\Omega}} = \sqrt{\frac{1}{V}}. \quad (34b)$$

With the above parameters, the molecular dipole and its derivatives [Eqs. (32) and (33)] become

$$d_{g,k\lambda}^{\text{sub}} = \sum_{\alpha} Q_\alpha \mathbf{R}_\alpha \cdot \boldsymbol{\xi}_\lambda, \quad (35a)$$

and

$$\frac{\partial d_{g,k\lambda}^{\text{sub}}}{\partial R_{\alpha i}} = Q_\alpha \mathbf{e}_i \cdot \boldsymbol{\xi}_\lambda, \quad (35b)$$

which are identical to previous work.<sup>33</sup> Hence, the current implementation is consistent with previous CavMD work with a single cavity mode.

### 7. Path-integral simulations of nuclear and photonic quantum effects

Before ending this section, we briefly discuss how to include quantum effects in mesoscale CavMD simulations. Although the above equations of motion in Eq. (28) are classical, nuclear and photonic quantum effects can also be captured by performing path-integral simulations.<sup>42,43</sup> After all, in Eq. (28), photons behave just like additional ‘‘nuclei’’. Hence, one can directly apply different flavors of path-integral approaches developed over the past decades<sup>54</sup> to study VSC.

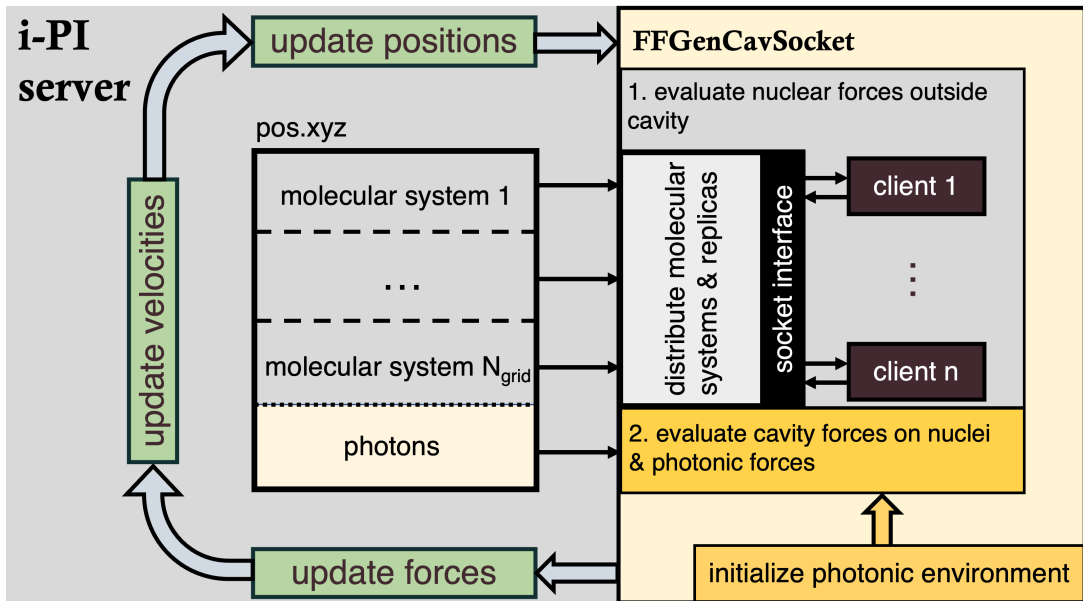


FIG. 3. A sketch of the mesoscale CavMD scheme as implemented in i-PI. The original i-PI server is responsible for updating the positions and velocities of the entire molecular + photonic system. The newly implemented **FFGenCavSocket** method, which stands for the force field **socket** interface for a **general cavity** setup, evaluates the forces for the whole system, including both the nuclear forces at different grid points (as shown in Fig. 2c) and the photonic forces. In path-integral simulations with  $P$  beads, the **FFGenCavSocket** method can connect to  $N_{\text{grid}} \times P$  different clients in parallel, thus significantly reducing the gradient evaluation time.

### III. SIMULATION DETAILS

We implemented the mesoscale CavMD scheme in the open source package i-PI;<sup>55</sup> see the caption of Fig. 3 for a detailed description of the implementation. In particular, the forces of molecular systems at different grid points were evaluated in parallel by i-PI through the socket interface by connecting to multiple clients, which each run their own force evaluation code.

The implementation of our method was tested on various cavity setups. The sketch of these cavity setups and the corresponding parameters are shown in Fig. (4) and Table I. In each cavity setup, the whole molecular system was represented by  $N_{\text{grid}}$  grid points. In cavity #1-#4, because the grid points along the  $y$ -direction all located at the origin ( $y = 0$ ), as shown in Eq. (23), the mode functions along the  $x$ -direction vanished. In other words, in cavity #1-#4, cavity modes polarized along the  $x$ -direction were decoupled from the molecules. Throughout the paper, the cavity loss is set as zero. The method and results for including the cavity loss are briefly discussed in the Appendix.

Each grid point was assigned a periodic boundary condition box containing 36  $\text{CO}_2$  molecules, which were explicitly simulated. The molecular density of the box was set to  $1.101 \text{ g/cm}^3$ . The  $\text{CO}_2$  molecules were modeled with the same force field that was used in previous work, which has been validated against experimental data.<sup>45</sup> Intermolecular Coulombic interactions were calculated using Ewald summation.

For equilibrium classical simulations, the coupled cavity-molecular system was initially equilibrated for 20 ps under an NVT ensemble at 300 K, using a time step of 0.5 fs. A Langevin thermostat with a friction lifetime of 100 fs was attached to each particle (both photons and nuclei). After this equilibration simulation, 40 consecutive 20-ps NVE simulations were performed using a time step of 0.5 fs. At the beginning of each NVE simulation, the initial velocities of all particles were resampled with a Maxwell-Boltzmann distribution at 300 K. For nonequilibrium classical simulation of polariton-polariton scattering in cavity #1, given the 40 starting geometries of the above consecutive NVE simulation, the  $y$ -coordinate of the  $l_x = 12$  cavity mode was displaced by 100 Å to represent an initially excited cavity mode. With each of these perturbed geometries, a 20-ps NVE simulation was performed.

For equilibrium path integral simulations, the thermostatted ring polymer molecular dynamics (TRPMD) approach was used.<sup>56</sup> While the simulation conditions of TRPMD largely resemble the classical case, here the difference is highlighted. We initialized the ring polymer with 4 beads for all nuclei and cavity photons with a time step of 0.25 fs. During all TRPMD simulations, a path integral Langevin equation (PILE) thermostat<sup>56</sup> was attached to the internal modes of the ring polymer with an optimally damped coefficient  $\lambda = 1/2$ .

Outside the cavity, the IR spectrum of liquid  $\text{CO}_2$  was calculated by Fourier transforming the dipole autocorre-

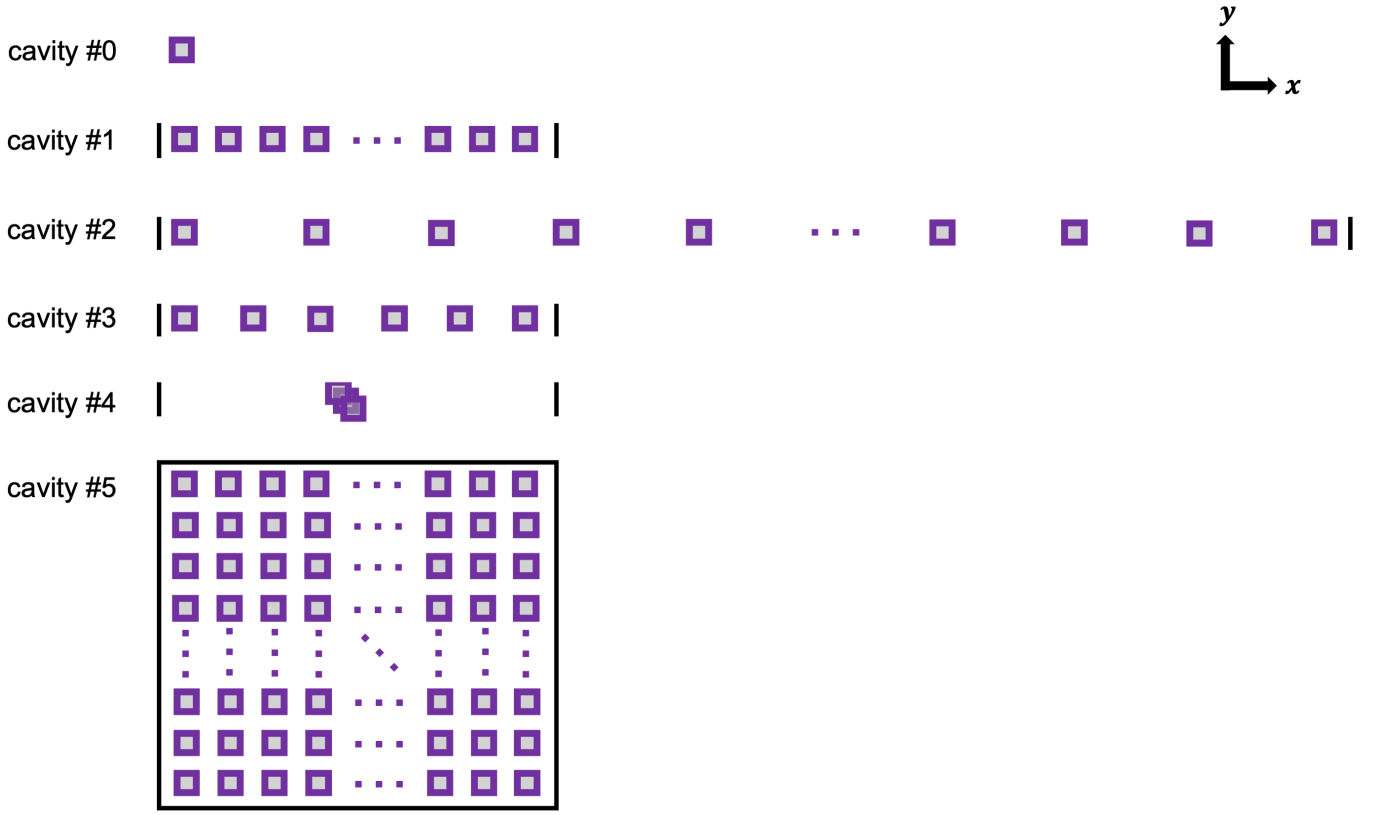


FIG. 4. Sketch of different cavity setups. Cavity #0 represents the standard cavity setup in previous CavMD simulations, where a large ensemble of molecules is coupled to a single cavity mode. Cavity #1-#5 represent the five cavity setups simulated in this work; see Table I for the corresponding cavity parameters.

TABLE I. Parameters for different cavity setups.<sup>a</sup>

cavity	$\omega_{\perp}$ [cm <sup>-1</sup> ]	$\Delta\omega_x$ [cm <sup>-1</sup> ]	$\Delta\omega_y$ [cm <sup>-1</sup> ]	$l_x^{\max}$	$l_y^{\max}$	$N_{\text{grid}}$	$x$ grid positions [ $L_x$ ]	$y$ grid positions [ $L_y$ ]	$\tilde{\epsilon}$ [a.u.]
#1	2320	50	0	36	1	36	[0.027, 0.054, ..., 0.973]	[0.0]	$5 \times 10^{-5}$
#2	2320	16.67	0	108	1	36	[0.027, 0.054, ..., 0.973]	[0.0]	$5 \times 10^{-5}$
#3	2320	50	0	36	1	6	[0.143, 0.286, ..., 0.857]	[0.0]	$1.225 \times 10^{-4}$
#4	2320	50	0	36	1	36	[0.5, 0.5, ..., 0.5]	[0.0]	$5 \times 10^{-5}$
#5	2320	50	50	18	18	1296	[0.027, 0.054, ..., 0.973]	[0.027, 0.054, ..., 0.973]	$8.3 \times 10^{-6}$

<sup>a</sup> In the table,  $\Delta\omega_{x,y} = c\pi/L_{x,y}$ ;  $\Delta\omega_y = 0$  indicates  $L_y = \infty$ . Each array along the  $x$ - or  $y$ -directions represents the evenly spaced locations (in the units of  $L_x$  or  $L_y$ ) of the molecular grid points along the corresponding axis. For example, in cavity #1, [0.027, 0.054, ..., 0.973] represent the  $x$ -grid locations for  $N_{\text{grid}} = 36$  grids. At each grid point, 36 CO<sub>2</sub> molecules are explicitly simulated under periodic boundary conditions. Cavity #1-#4 represent four sets of parameters for 1D cavities, while cavity #5 simulates a 2D cavity.

lation function of the molecules:<sup>45,57-60</sup>

$$F(\omega) \propto \omega^2 \int_{-\infty}^{+\infty} dt e^{-i\omega t} \left\langle \sum_{i=x,y,z} \mu_i(0) \mu_i(t) \right\rangle. \quad (36)$$

Here,  $\mu_i(t)$  denotes the total dipole moment of the molecular system in each dimension.

Inside the cavity, the IR spectrum of the polaritons was calculated by evaluating the position autocorrelation function of the cavity photons:

$$F_{k\lambda}(\omega) \propto \omega^2 \int_{-\infty}^{+\infty} dt e^{-i\omega t} \langle \tilde{q}_{k\lambda}(0) \tilde{q}_{k\lambda}(t) \rangle. \quad (37)$$

## IV. RESULTS

### A. Cavity #1: An 1D approximation of planar Fabry-Pérot cavities

As shown in Fig. 4, cavity #1 contains 36 cavity modes as well as 36 evenly spaced grid points along the  $x$  direction. For such a 1D cavity setup, the cavity frequency dispersion relation reads

$$\omega_c(l_x) = \sqrt{\omega_{\perp}^2 + l_x^2 \Delta\omega_x^2}, \quad (38)$$

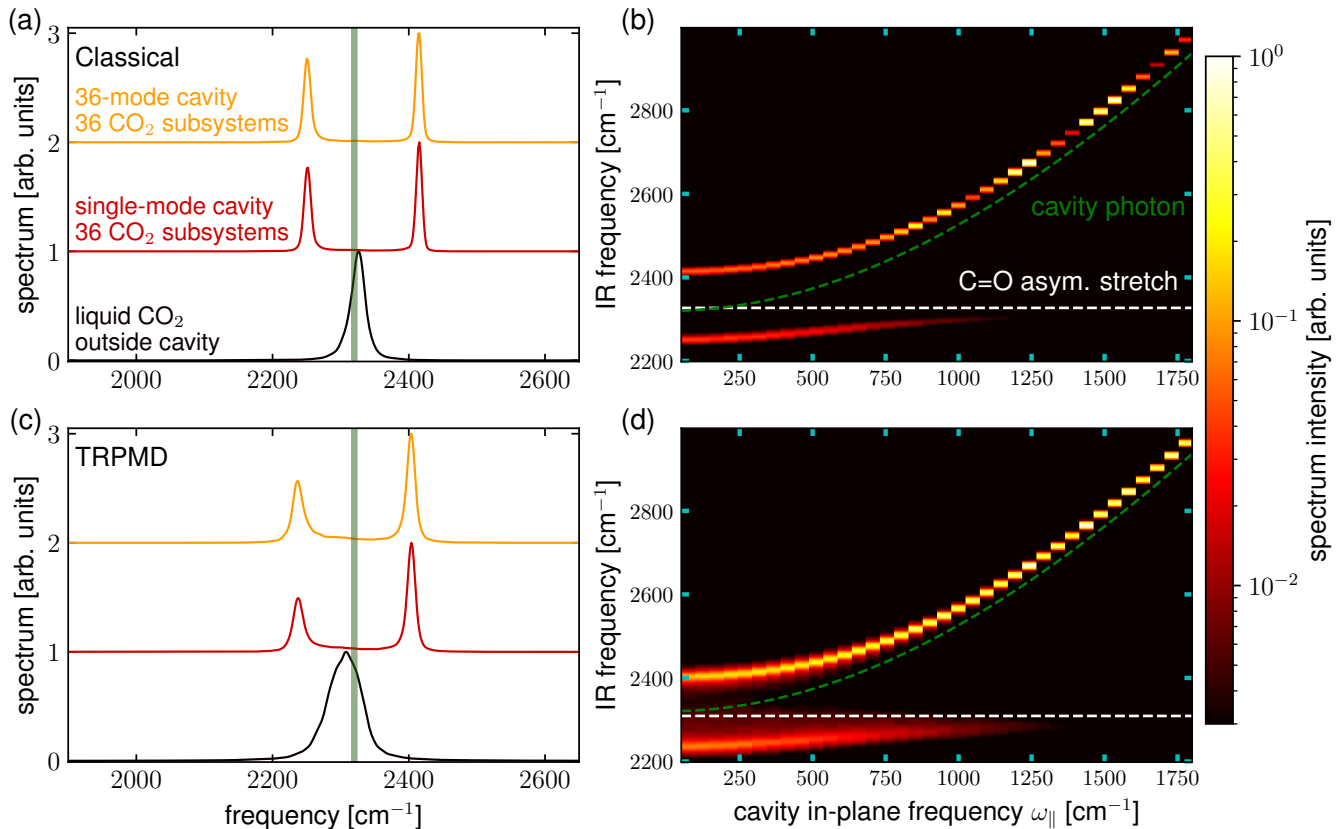


FIG. 5. Polariton spectra in a lossless cavity from classical (upper panel) or path-integral (bottom panel) CavMD simulations. (a) The normalized IR spectrum of liquid  $\text{CO}_2$  outside the cavity (black), coupled to a single-mode cavity (red), or a multimode Fabry–Pérot-like 1D cavity (cavity #1, yellow). The vertical green line denotes the cavity frequency at normal incidence (the lowest-frequency cavity mode). (b) The polariton spectrum vs the cavity in-plane frequency  $\omega_{\parallel}$  corresponding to the multimode cavity. (c, d) The same plot as the upper panel except that the TRPMD method is used to propagate the dynamics.

where  $\omega_{\perp} = 2320 \text{ cm}^{-1}$ ,  $\Delta\omega_x = 50 \text{ cm}^{-1}$ , and  $l_x = 1, 2, \dots, 36$ .

### 1. Polariton spectrum: the validity of the single-mode approximation

Fig. 5a shows the polariton spectrum (yellow line) of  $\text{CO}_2$  confined in this cavity, obtained from classical CavMD simulations. The yellow line represents the polariton spectrum formed between the asymmetric C=O stretch (black line) of liquid  $\text{CO}_2$  and the cavity photon mode at normal incidence (vertical green line). This polariton spectrum is calculated by taking the Fourier transform of the coordinate autocorrelation function of the lowest-frequency cavity mode (with  $l_x = 1$ ). If only a single cavity mode at  $l_x = 1$  is included in the simulation, the resulting polariton spectrum (red line) is identical to that of the 36-mode cavity #1. This agreement shows the validity of using the single-mode approximation for describing the linear-response polariton spectrum: cavity modes at different  $\omega_{\parallel}$  values effectively do not interact with each other. Of course, for cavity #1, when the

coordinate autocorrelation functions of cavity modes at different  $\omega_{\parallel}$  are evaluated, the well-known  $\omega_{\parallel}$ -dependent upper and lower polariton (UP and LP) branches<sup>11,13</sup> can be recovered, as shown in Fig. 5b.

The lower panel of Fig. 5 provides analogous results when a TRPMD simulation is performed. Compared with the classical results in the upper panel, both the polariton peaks and the C=O asymmetric stretch are slightly red-shifted. The broadening of the peaks, as suggested by Ref. 43, may be attributed to the artifacts in TRPMD rather than a real quantum effect. Because there is no significant difference between the classical and TRPMD results, for the calculations below, only classical simulations will be performed.

### 2. Polariton-polariton scattering beyond the single-mode approximation

Fig. 6a elaborates further on the 36-mode simulation, when the cavity mode at  $l_x = 12$  (corresponding to  $\omega_c = 2396 \text{ cm}^{-1}$ ) is strongly excited at  $t = 0$ . The red line plots the photon energy dynamics of this initially

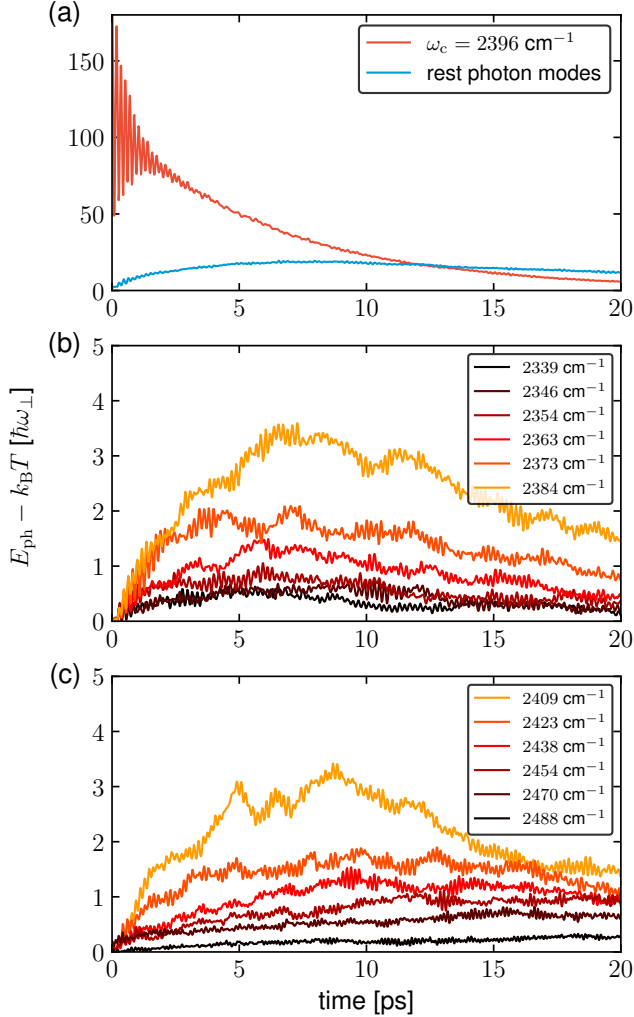


FIG. 6. Nonequilibrium photon energy dynamics in the cavity #1 setup when the cavity mode at  $\omega_c = 2396 \text{ cm}^{-1}$  ( $l_x = 12$ ) is initially excited. (a) Photon energy dynamics for the initially excited cavity mode (red line) vs. the summed photon energy of the remaining photon modes with  $l_x \neq 12$  (blue line). (b,c) The photon energy dynamics for cavity modes with frequency (b)  $\omega_c < 2396 \text{ cm}^{-1}$  or (c)  $\omega_c > 2396 \text{ cm}^{-1}$ . Here, lines with yellow (black) colors represent cavity modes with frequencies close to (far from) the initially excited photon mode. Energy scattering occurs from the initially excited photon mode to the neighboring cavity modes at different  $\omega_{\parallel}$ .

excited cavity mode, while the blue line ( $l_x \neq 12$ ) plots the summed photon energy of the other cavity modes. In general, the excited cavity photon relaxes to the ground state within 10 ps, and the other cavity modes absorb energy transiently up to  $t = 5 \sim 10$  ps and then dissipate their energy at later times. The dissipation of photon energy stems from polariton energy transfer to the dark modes, as the cavity loss is set to zero during our simulations. Please note that since the photon excitation at  $\omega_c = 2396 \text{ cm}^{-1}$  is implemented by displacing the photon coordinate at time  $t = 0$ , both the UP and LP have

been equally excited. Hence, the excited photon exhibits a strong Rabi oscillation pattern initially ( $t < 2$  ps). At later times, however, the Rabi oscillations disappear, as the LP lifetime is shorter than the UP lifetime;<sup>44,45</sup> therefore, only the UP signal remains.

To better understand the dynamics of the remaining photon modes ( $l_x \neq 12$ ), in Figs. 6b,c, we further provide the photon energy dynamics of each of these photon modes. Lines in yellow represent cavity modes with frequencies close to the excited photon frequency ( $\omega_c = 2396 \text{ cm}^{-1}$ ), and lines with deeper colors represent cavity modes with frequencies further from it. Clearly, among all of the remaining cavity modes, the closer the frequency to the initially excited photon mode, the more energy the initially unexcited cavity photon receives transiently. This frequency-dependent transient excitation indicates polariton-polariton scattering, a fundamental mechanism that has been widely studied both experimentally and theoretically in planar Fabry-Pérot cavities.<sup>34</sup> Because molecules interact with each other, interactions among polaritons with different  $\omega_{\parallel}$  values, which are hybrid light-matter states that can be viewed as molecular excitations modulated by cavity modes, can indeed occur.

As a short summary, although linear-response polariton spectra seem to suggest that the single-mode approximation is valid, nonequilibrium CavMD simulations emphasize that including  $\omega_{\parallel}$ -dependent cavity modes is critical for accurately modeling the dynamics of polariton-polariton scattering events.

## B. 1D Cavity setups which cannot be used to represent Fabry-Pérot cavities

The example of cavity #1 above represents a set of parameters that could be used to model realistic Fabry-Pérot cavities. However, it is also useful to investigate under which conditions the numerical scheme cannot be used to simulate realistic Fabry-Pérot cavities. To this end, we now consider such three additional sets of cavity parameters, labeled as cavity #2-#4.

### 1. Cavity #2

As shown in Table I, when compared to cavity #1, cavity #2 includes more cavity modes (108 instead of 36) and a smaller  $\Delta\omega_x$  ( $16.67 \text{ cm}^{-1}$  instead of  $50 \text{ cm}^{-1}$ ). The physical meaning of reducing  $\Delta\omega_x$  is demonstrated in Fig. 4: a larger  $L_x$  and a sparser distribution of the molecular grid points along the  $x$ -direction (the cavity mirror plane).

Fig. 7a plots the polariton spectrum at normal incidence (yellow line) for this 108-mode cavity. The polariton spectrum is red-shifted compared to the case when only the lowest-frequency cavity mode (with  $l_x = 1$ , red line) is included in the simulation. This difference indi-

cates the breakdown of the single-mode approximation. More obviously, as shown in Fig. 7b, the  $\omega_{\parallel}$ -dependent polariton spectrum exhibits a much more complicated polariton structure than Fig. 5b: here four polariton branches exist in the spectrum, with multiple avoided crossings.

## 2. Cavity #3

For another example, cavity #3 also resembles cavity #1 except here a smaller number of molecular grid points, 6 (instead of 36), are evenly distributed. In order to guarantee a similar Rabi splitting as cavity #1, the effective light-matter coupling  $\tilde{\epsilon}$  would need to be increased by a factor of  $\sqrt{6}$ , from  $5 \times 10^{-5}$  a.u. to  $1.225 \times 10^{-4}$  a.u.

Fig. 8a plots the corresponding polariton spectrum at normal incidence (yellow line). This spectrum contains four polariton peaks, which is very different from the case of a single-mode cavity, i.e., when only the lowest-frequency cavity mode ( $l_x = 1$ ) is included in the simulation (red line). Moreover, in the  $\omega_{\parallel}$ -dependent polariton spectrum (Fig. 8b), cavity #3 exhibits an even more complicated polariton spectrum than Fig. 7b, thus strongly indicating significant interaction between cavity photons at different  $\omega_{\parallel}$ .

## 3. Cavity #4

Lastly, consider an extreme example — cavity #4. Here, all molecular grid points are accumulated at the middle of the cavity mirror plane (along the  $x$ -direction), while all the other parameters remain the same as cavity #1. This cavity setup could be regarded as a naive generalization of the single-mode Pauli-Fierz Hamiltonian to the multi-mode case. For this cavity, the corresponding polariton spectrum, as illustrated in Fig. 9, becomes very complicated. As shown in Fig. 9a, many peaks coexist in the polariton spectrum at normal incidence (yellow line). Moreover, in the  $\omega_{\parallel}$ -dependent polariton spectrum (Fig. 9b), any well-defined polariton branch or avoided crossing completely disappears. Hence, cavity #4 fails completely to mimic the polariton dispersion relation in VSC experiments. This failure emphasizes the fact that the long-wave approximation (i.e., approximating the whole molecular system as localized at a single point) fails when including many  $\omega_{\parallel}$ -dependent cavity modes.

## C. Cavity #5: a 2D cavity setup

After demonstrating the results for several 1D cavities, we found that only the parameter set for cavity #1 can be used to represent Fabry-Pérot cavities. However, given that most VSC experiments thus far have employed 2D Fabry-Pérot cavities, it is critical to further evaluate the capabilities of our code by directly simulating 2D cavities.

After all, the photonic density of states for 1D cavities differ significantly from that for 2D cavities.

As shown in Fig. 4 and Table I, cavity #5 extends the parameter set of cavity #1 to 2D, i.e., with a 2D molecular grid of size  $36 \times 36$  (1296 sample points). For such a 2D cavity setup, the cavity frequencies can take

$$\omega_c(l_x, l_y) = \sqrt{\omega_{\perp}^2 + l_x^2 \Delta\omega_x^2 + l_y^2 \Delta\omega_y^2}, \quad (39)$$

where  $\omega_{\perp} = 2320 \text{ cm}^{-1}$ ,  $\Delta\omega_{x,y} = 50 \text{ cm}^{-1}$ , and  $l_{x,y} = 1, 2, \dots, 18$ .

Fig. 10 plots the polariton dispersion relation of cavity #5 after an equilibrium CavMD simulation. We fix  $\omega_y \equiv l_y \Delta\omega_y$  and plot  $\omega_x \equiv l_x \Delta\omega_x$  for several values of  $\omega_y$ : (a)  $50 \text{ cm}^{-1}$ , (b)  $550 \text{ cm}^{-1}$ , and (c)  $900 \text{ cm}^{-1}$ . As  $\omega_y$  is increased, the three subplots of the polariton dispersion relation show the transition from on-resonance strong coupling at  $\omega_x \approx 0$  to complete off-resonance. Clearly, cavity #5 can be regarded as a 2D model of realistic planar Fabry-Pérot cavities.

## V. DISCUSSION

After performing simulations on cavity #1-#5, we have learned that obtaining a numerical solution to VSC in planar Fabry-Pérot cavities is nontrivial. On the one hand, the computational cost must be bearable in the simulation of Fabry-Pérot VSC. To this end, both the cavity modes at different  $\omega_{\parallel}$  and the molecular distribution need to be discretized. On the other hand, an inappropriate discretization scheme may break the single-mode approximation and produce inconsistent results when compared with experiments. Hence, one must wonder which discretization scheme is valid.

### A. The role of in-plane translational symmetry in planar Fabry-Pérot cavities

Before discussing how to prepare an appropriate discretization scheme, let us briefly review the reason why the single-mode approximation is valid to describe the linear-response polariton spectrum in planar Fabry-Pérot cavities. As discussed before, the polariton eigenvalues in a planar Fabry-Pérot cavity can be obtained by solving the eigenequation below:<sup>61</sup>

$$\alpha(\mathbf{k}_{\parallel})[\omega - \omega_c(k_{\parallel})] = \sum_i T_i^*(\mathbf{k}_{\parallel}) \sum_{\mathbf{k}'_{\parallel}} T_i(\mathbf{k}'_{\parallel}) \alpha(\mathbf{k}'_{\parallel}) / [\omega - \omega_0]. \quad (40)$$

Here,  $|\alpha(\mathbf{k}_{\parallel})|^2$  denotes the photonic weight of the polaritons at  $\mathbf{k}_{\parallel}$ ;  $\omega_0$  denotes the molecular excitation frequency;  $T_i(\mathbf{k}_{\parallel})$  denotes the light-matter coupling between the cavity photon mode at  $\mathbf{k}_{\parallel}$  and the  $i$ -th molecule. Although the explicit form of  $T_i(\mathbf{k}_{\parallel})$  can be multivariate,<sup>61</sup> we are interested only in its dependence on the in-plane

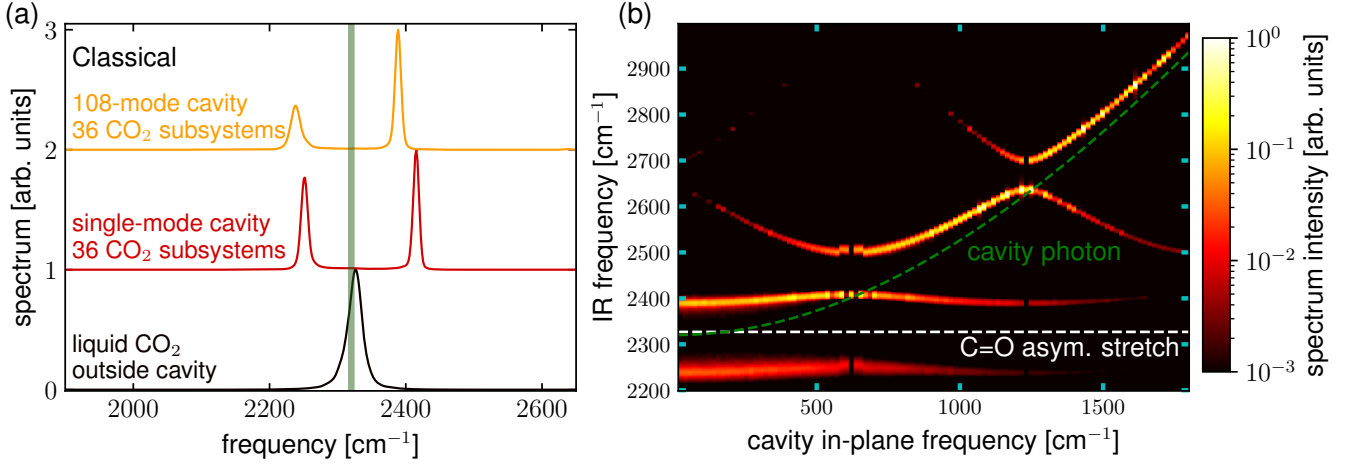


FIG. 7. Similar plots as Figs. 5a,b except that cavity #1 is replaced by cavity #2; i.e., 108 (instead of 36) cavity modes are used during the simulation.

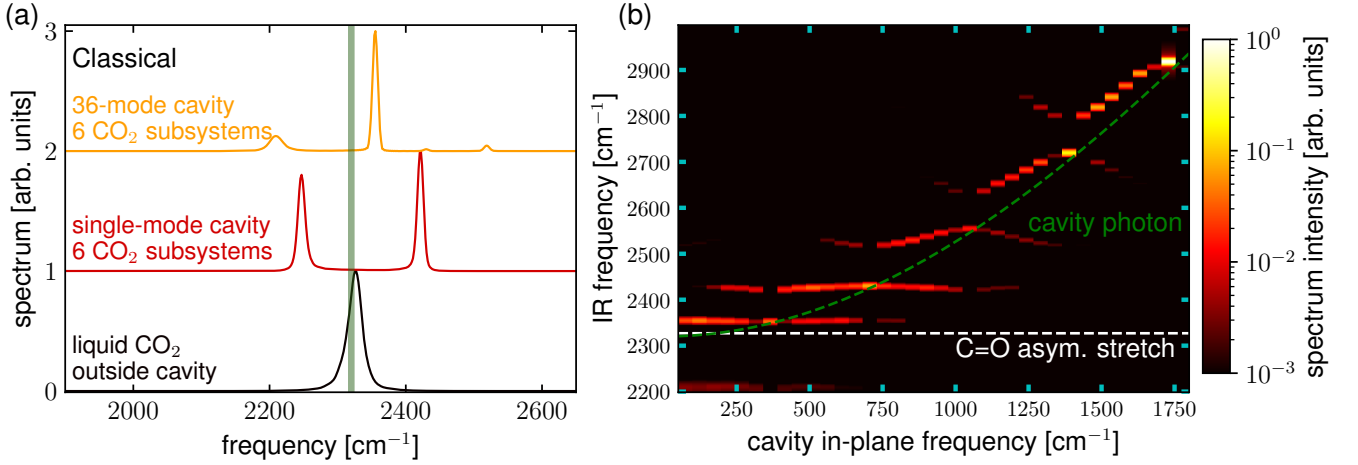


FIG. 8. Similar plots as Figs. 5a,b except that here cavity #1 is replaced by cavity #3; i.e., only  $N_{\text{grid}} = 6$  (instead of  $N_{\text{grid}} = 36$ ) grid points are used during the simulation and the molecular distribution along the cavity mirror plane (the  $x$ -direction) becomes very sparse.

phase of the cavity modes. To this end, we can write

$$T_i(\mathbf{k}_{\parallel}) = T_i e^{i\mathbf{k}_{\parallel} \cdot \mathbf{r}_{\parallel}^{(i)}}, \quad (41)$$

where  $T_i$  denotes the prefactor, and  $\mathbf{r}_{\parallel}^{(i)}$  denotes the molecule position along the cavity mirror plane. Assuming  $T_i$  as a constant and  $\alpha(\mathbf{k}_{\parallel}) \approx \alpha(\mathbf{k}'_{\parallel})$ , we can rewrite Eq. (40) as

$$[\omega - \omega_c(k_{\parallel})][\omega - \omega_0] \approx \sum_i \sum_{\mathbf{k}'_{\parallel}} |T_i|^2 e^{-i(\mathbf{k}_{\parallel} - \mathbf{k}'_{\parallel}) \cdot \mathbf{r}_{\parallel}^{(i)}}. \quad (42)$$

Given a homogeneous distribution of molecules along the cavity mirror plane, the summation in Eq. (42) over  $\mathbf{k}'_{\parallel} \neq \mathbf{k}_{\parallel}$  should cancel out with each other. Mathematically speaking, the translational symmetry

along the cavity mirror plane gives  $\sum_i e^{-i(\mathbf{k}_{\parallel} - \mathbf{k}'_{\parallel}) \cdot \mathbf{r}_{\parallel}^{(i)}} \propto \int d\mathbf{r}_{\parallel} e^{-i(\mathbf{k}_{\parallel} - \mathbf{k}'_{\parallel}) \cdot \mathbf{r}_{\parallel}} \propto \delta(\mathbf{k}_{\parallel} - \mathbf{k}'_{\parallel})$ , i.e., the summation  $\sum_i$  can be replaced by a simple integral  $\int d\mathbf{r}_{\parallel}$  only when the molecular distribution is homogeneous along the cavity mirror plane. Hence, Eq. (42) becomes

$$[\omega - \omega_c(k_{\parallel})][\omega - \omega_0] = \text{const.} \quad (43)$$

Eq. (43) is the polariton eigenequation under the single-mode approximation, i.e., the cavity modes at different  $k_{\parallel}$  effectively do not interact with each other. Note that to derive Eq. (43) from Eq. (42), we must apply the in-plane translational symmetry.

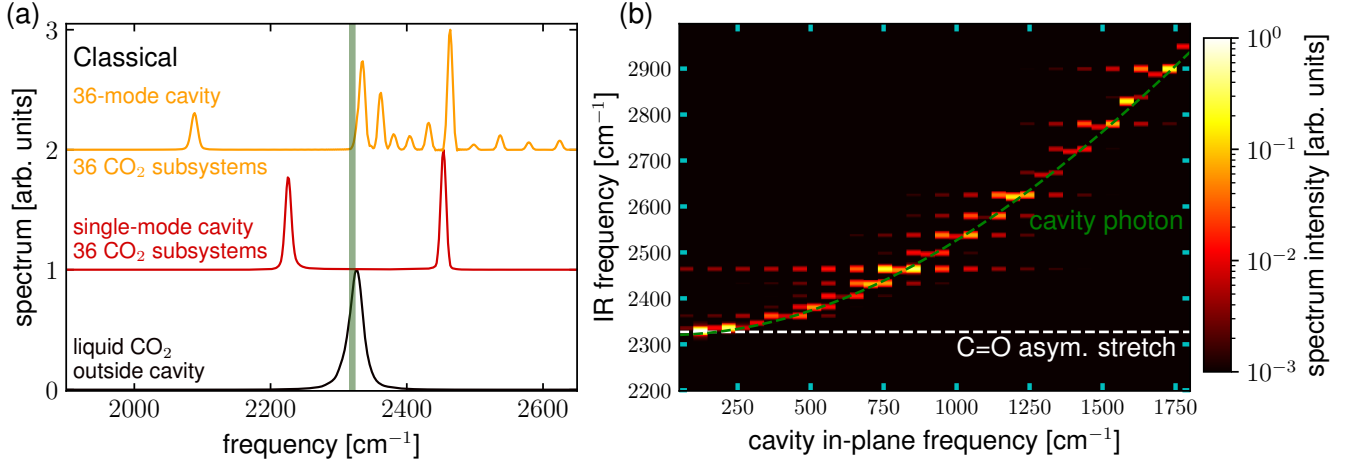


FIG. 9. Similar plots as Figs. 5a,b except that here cavity #1 is replaced by cavity #4; i.e., the spatial variance of different molecular grid points is eliminated and the long wave approximation is taken.

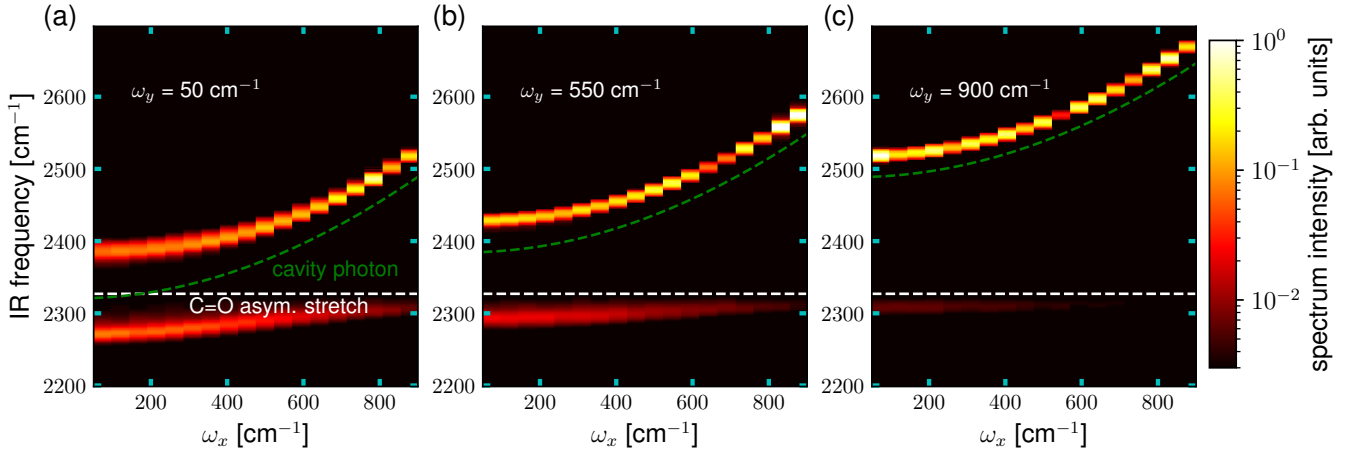


FIG. 10. The polariton dispersion relation for cavity #5 as a function of  $\omega_x \equiv l_x \Delta \omega_x$ , the in-plane frequency along the  $x$ -direction, when  $\omega_y \equiv l_y \Delta \omega_y$  is chosen as (a)  $50 \text{ cm}^{-1}$ , (b)  $550 \text{ cm}^{-1}$ , and (c)  $900 \text{ cm}^{-1}$ .

## B. How to satisfy in-plane translational symmetry numerically?

As shown above, the (continuous) in-plane translational symmetry is the key to obtain the polariton eigenequation under the single-mode approximation. In our simulations, both the cavity modes at different  $\omega_{\parallel}$  and the molecular distribution are discretized, so the continuous in-plane translational symmetry is of course no longer preserved.

However, the loss of continuous in-plane translational symmetry does not preclude numerical simulation of planar Fabry-Pérot cavities. Instead, we believe that preserving discrete in-plane translational symmetry is adequate. For our 1D Fabry-Pérot-like cavity setups, analogous to the cancellation of the  $\mathbf{k}'_{\parallel} \neq \mathbf{k}_{\parallel}$  terms in Eq. (42),

it is necessary to reduce the following error function

$$\text{Err}(k_x) = \frac{1}{N_{\text{grid}}} \sum_{i=1}^{N_{\text{grid}}} \sum_{k'_x \neq k_x} \sin(k'_x x_i) \sin(k_x x_i) \rightarrow 0 \quad (44)$$

to zero for any given  $k_x$ , where  $x_i$  denotes the location of the  $i$ -th grid point.

Given the parameters of the cavity setups in Table I, in Table II we provide the statistics of the error function  $\text{Err}(k_x)$  for each 1D cavity setup. While, for cavity #1,  $\text{Err}(k_x)$  is always exactly equal to zero for arbitrary  $k_x$ , for cavities #2, #3, and #4, a finite percentage of  $\text{Err}(k_x)$  has been found to be non-zero for various  $k_x$  values. Because we have learned that only cavity #1 can be used to represent Fabry-Pérot cavities employed in experiments, Eq. (44) appears to be a good criterion to check whether the discrete translational symmetry is

TABLE II. Statistics of  $\text{Err}(k_x)$  [Eq. (44)] for the 1D cavity setups.

cavity	$\langle  \text{Err}(k_x)  \rangle$	percentage of $\text{Err}(k_x) \neq 0$
#1	0.00	0%
#2	0.34	35%
#3	0.42	44%
#4	0.50	50%

satisfied for the numerical setups of 1D cavities. Moreover, Table II appears to indicate that both the absolute average  $\langle |\text{Err}(k_x)| \rangle$  and the percentage of the non-zero  $\text{Err}(k_x)$  may have a positive correlation with the breakdown of the single-mode approximation: the larger these values, the less the polariton dispersion relation is consistent with experimental findings.

In summary, to numerically simulate 1D Fabry–Pérot cavities, which we can use to interpret experiments, we need to guarantee Eq. (44). Of course, it is also necessary to have a sufficient number of photon modes as well as molecular grid points. Although our discussion above focused on 1D cavities, the conclusion can also be generalized to 2D cavities. It appears that to numerically preserve the translational symmetry of 2D cavities (e.g., cavity #5), one just needs to make sure the cavity parameters for each dimension preserve the discrete translational symmetry [Eq. (44)] independently.

### C. Do cavities in the absence of in-plane translational symmetry have physical meaning?

With the above discussion in mind, one may treat cavity #2-#4 as a few (unphysical) counterexamples of how to not conserve the in-plane translational symmetry. However, we also want to emphasize that cavity #2-#4 could have real physical meaning. In experiments, if one could prepare cavities with two sets of parallel cavity mirrors along both  $z$ - and  $x$ -directions and then distribute molecules (probably in the solid state) in a similar manner as in cavity #2-#4 (see Fig. 4), one might be able to observe the complicated polariton spectra as shown in Figs. 7-9. These complicated polariton spectra might provide a flexible approach for controlling polariton-polariton scattering and may find wide applications in the future. Even for 2D Fabry–Pérot cavities used in experiments, by nonuniformly distributing molecules along the cavity mirror plane, one could also observe very complicated polariton dispersion relations. A more comprehensive investigation in this direction is reported elsewhere.

## VI. CONCLUSION

To summarize, we have provided a mesoscale CavMD formalism for studying VSC with Fabry–Pérot-like cavi-

ties. As this formalism is derived from a general Power–Zienau–Woolley Hamiltonian, our CavMD scheme is gauge invariant and can be easily extended to more complicated photonic environments. The examples of cavities #1-#5 showcase the importance of preserving the in-plane translational symmetry for capturing the  $\omega_{\parallel}$ -dependent polariton branches observed in experiments. Additionally, our nonequilibrium CavMD simulations have provided initial evidence of elastic vibrational polariton-polariton scattering at nearest neighbor  $\omega_{\parallel}$ .

With this fundamental mechanism in mind, in future work, CavMD could be used as a numerical tool to investigate vibrational polariton transport<sup>40</sup> and explore the experimental conditions necessary to prepare vibrational polariton condensates,<sup>62</sup> theoretical hypotheses that have not been experimentally observed. In addition, this code can be used to numerically examine various hypotheses on the origin of the VSC catalytic effects observed in the Ebbesen experiments.

In the end, we emphasize that the simulation results for cavities #2-#4 also highlight a research opportunity. Specifically, if the molecular distribution along the cavity mirror plane does not preserve the in-plane translational symmetry, more complicated  $k_{\parallel}$ -dependent polariton dispersion relations could be experimentally observed. Such a possible avenue is worthy of further investigation, as it provides more flexibility to tune polariton-polariton interactions at different  $k_{\parallel}$  values than conventional homogeneous Fabry–Pérot cavities.

## VII. ACKNOWLEDGMENTS

This material is based upon the work supported by the start-up funds from the University of Delaware Department of Physics and Astronomy. This research is also supported in part through the use of Information Technologies (IT) resources at the University of Delaware, specifically the high-performance computing resources.

## VIII. DATA AVAILABILITY STATEMENT

The data that support the findings of this study, including the source code, input and post-processing scripts, and the corresponding tutorials, will be available at Github upon publication of the manuscript.

### Appendix A: Including cavity loss

The cavity loss has been turned off throughout the calculations above. As a side note, here we briefly discuss the effects of cavity loss on our simulations. Overall, including cavity loss is very straightforward within the framework of CavMD<sup>53</sup> — the photonic equation of motion in Eq. (28b) needed to be replaced by the following

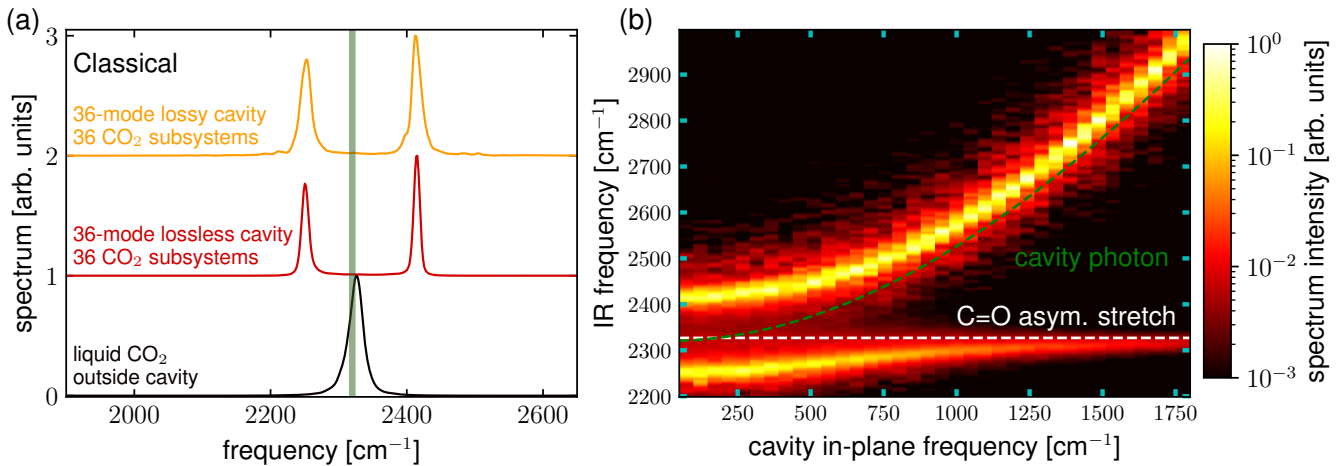


FIG. 11. Polariton spectra from classical CavMD simulations. (a) The normalized IR spectrum of liquid CO<sub>2</sub> outside the cavity (black), coupled to a 36-mode lossless cavity (red, Fig. 5a), or a 36-mode lossy cavity with the cavity lifetime as  $1/\gamma_{k\lambda} \equiv 300$  fs (yellow). (b) The polariton spectrum vs the cavity in-plane frequency  $\omega_{\parallel}$  corresponding to the lossy 36-mode cavity. The simulation conditions inside the 36-mode cavity are identical to those in Figs. 5a,b (cavity #1).

form:

$$m_{k\lambda} \ddot{q}_{k\lambda} = -m_{k\lambda} \omega_k^2 \tilde{q}_{k\lambda} - \tilde{\varepsilon}_{k\lambda} q_{g,k\lambda}^{\text{sub}} - \gamma_{k\lambda} \dot{p}_{k\lambda} + \eta_{k\lambda}(t), \quad (\text{A1})$$

where  $\gamma_{k\lambda}$  and  $\eta_{k\lambda}(t)$  denote the damping rate and the Langevin white noise for each cavity mode, respectively. In other words, a standard Langevin thermostat is attached on top of each cavity mode.

Fig. 11a plots the polariton spectrum at normal incidence corresponding to the cavity #1 in Fig. 5a when the cavity lifetime is set as  $1/\gamma_{k\lambda} \equiv 300$  fs (yellow line). Here, the polariton linewidth is broadened as compared to the case of the lossless cavity (red line). The polariton dispersion relation in Fig. 11b also obviously demonstrates the polariton linewidth broadening in the lossy cavity. Note that when the simulation trajectories were used to calculate the polariton spectra in the lossy cavity, only the cavity modes (not molecules) were coupled to the Langevin thermostat.

<sup>1</sup>A. Shalabney, J. George, J. Hutchison, G. Pupillo, C. Genet, and T. W. Ebbesen, “Coherent Coupling of Molecular Resonators with a Microcavity Mode,” *Nat. Commun.* **6**, 5981 (2015).

<sup>2</sup>J. P. Long and B. S. Simpkins, “Coherent Coupling between a Molecular Vibration and Fabry–Perot Optical Cavity to Give Hybridized States in the Strong Coupling Limit,” *ACS Photonics* **2**, 130–136 (2015).

<sup>3</sup>A. Thomas, J. George, A. Shalabney, M. Dryzhakov, S. J. Varma, J. Moran, T. Chervy, X. Zhong, E. Devaux, C. Genet, J. A. Hutchison, and T. W. Ebbesen, “Ground-State Chemical Reactivity under Vibrational Coupling to the Vacuum Electromagnetic Field,” *Angew. Chemie Int. Ed.* **55**, 11462–11466 (2016).

<sup>4</sup>A. D. Dunkelberger, B. T. Spann, K. P. Fears, B. S. Simpkins, and J. C. Owrutsky, “Modified Relaxation Dynamics and Coherent Energy Exchange in Coupled Vibration-Cavity Polaritons,” *Nat. Commun.* **7**, 1–10 (2016).

<sup>5</sup>A. Thomas, L. Lethuillier-Karl, K. Nagarajan, R. M. A. Vergauwe, J. George, T. Chervy, A. Shalabney, E. Devaux, C. Genet, J. Moran, and T. W. Ebbesen, “Tilting a Ground-State Reactivity Landscape by Vibrational Strong Coupling,” *Science* **363**, 615–619 (2019).

<sup>6</sup>B. Xiang, R. F. Ribeiro, M. Du, L. Chen, Z. Yang, J. Wang, J. Yuen-Zhou, and W. Xiong, “Intermolecular Vibrational Energy Transfer Enabled by Microcavity Strong Light–Matter Coupling,” *Science* **368**, 665–667 (2020).

<sup>7</sup>T.-T. Chen, M. Du, Z. Yang, J. Yuen-Zhou, and W. Xiong, “Cavity-enabled Enhancement of Ultrafast Intramolecular Vibrational Redistribution over Pseudorotation,” *Science* **378**, 790–794 (2022).

<sup>8</sup>W. Ahn, J. F. Triana, F. Recabal, F. Herrera, and B. S. Simpkins, “Modification of Ground-State Chemical Reactivity via Light–Matter Coherence in Infrared Cavities,” *Science* **380**, 1165–1168 (2023).

<sup>9</sup>A. D. Wright, J. C. Nelson, and M. L. Weichman, “Rovibrational Polaritons in Gas-Phase Methane,” *J. Am. Chem. Soc.* **145**, 5982–5987 (2023).

<sup>10</sup>R. F. Ribeiro, L. A. Martínez-Martínez, M. Du, J. Campos-Gonzalez-Angulo, and J. Yuen-Zhou, “Polariton Chemistry: Controlling Molecular Dynamics with Optical Cavities,” *Chem. Sci.* **9**, 6325–6339 (2018).

<sup>11</sup>T. E. Li, B. Cui, J. E. Subotnik, and A. Nitzan, “Molecular Polaritons: Chemical Dynamics Under Strong Light–Matter Coupling,” *Annu. Rev. Phys. Chem.* **73**, 43–71 (2022).

<sup>12</sup>J. Fregoni, F. J. Garcia-Vidal, and J. Feist, “Theoretical Challenges in Polaritonic Chemistry,” *ACS Photonics* **9**, 1096–1107 (2022).

<sup>13</sup>B. S. Simpkins, A. D. Dunkelberger, and I. Vurgaftman, “Control, Modulation, and Analytical Descriptions of Vibrational Strong Coupling,” *Chem. Rev.* **123**, 5020–5048 (2023).

<sup>14</sup>A. Mandal, M. A. Taylor, B. M. Weight, E. R. Koessler, X. Li, and P. Huo, “Theoretical Advances in Polariton Chemistry and Molecular Cavity Quantum Electrodynamics,” *Chem. Rev.* **123**, 9786–9879 (2023).

<sup>15</sup>M. Ruggenthaler, D. Sidler, and A. Rubio, “Understanding Polaritonic Chemistry from Ab Initio Quantum Electrodynamics,” *Chem. Rev.* **123**, 11191–11229 (2023), arXiv:2211.04241.

<sup>16</sup>M. V. Imperatore, J. B. Asbury, and N. C. Giebink, “Reproducibility of Cavity-Enhanced Chemical Reaction Rates in the Vibrational Strong Coupling Regime,” *J. Chem. Phys.* **154**, 191103 (2021).

<sup>17</sup>G. D. Wiesehan and W. Xiong, “Negligible Rate Enhancement from Reported Cooperative Vibrational Strong Coupling Catalysis,” *J. Chem. Phys.* **155**, 241103 (2021).

<sup>18</sup>A. P. Fidler, L. Chen, A. M. McKillop, and M. L. Weichman,

- “Ultrafast Dynamics of CN Radical Reactions with Chloroform Solvent Under Vibrational Strong Coupling,” arXiv (2023), arXiv:2307.04875.
- <sup>19</sup>J. Galego, C. Climent, F. J. Garcia-Vidal, and J. Feist, “Cavity Casimir-Polder Forces and Their Effects in Ground-State Chemical Reactivity,” *Phys. Rev. X* **9**, 021057 (2019).
- <sup>20</sup>J. A. Campos-Gonzalez-Angulo, R. F. Ribeiro, and J. Yuen-Zhou, “Resonant Catalysis of Thermally Activated Chemical Reactions with Vibrational Polaritons,” *Nat. Commun.* **10**, 4685 (2019).
- <sup>21</sup>N. M. Hoffmann, L. Lacombe, A. Rubio, and N. T. Maitra, “Effect of Many Modes on Self-Polarization and Photochemical Suppression in Cavities,” *J. Chem. Phys.* **153**, 104103 (2020).
- <sup>22</sup>X. Li, A. Mandal, and P. Huo, “Cavity Frequency-Dependent Theory for Vibrational Polariton Chemistry,” *Nat. Commun.* **12**, 1315 (2021).
- <sup>23</sup>E. W. Fischer and P. Saalfrank, “Ground State Properties and Infrared Spectra of Anharmonic Vibrational Polaritons of Small Molecules in Cavities,” *J. Chem. Phys.* **154**, 104311 (2021).
- <sup>24</sup>P. Y. Yang and J. Cao, “Quantum Effects in Chemical Reactions under Polaritonic Vibrational Strong Coupling,” *J. Phys. Chem. Lett.* **12**, 9531–9538 (2021).
- <sup>25</sup>D. S. Wang, T. Neuman, S. F. Yelin, and J. Flick, “Cavity-Modified Unimolecular Dissociation Reactions via Intramolecular Vibrational Energy Redistribution,” *J. Phys. Chem. Lett.* **13**, 3317–3324 (2022).
- <sup>26</sup>J. Flick, M. Ruggenthaler, H. Appel, and A. Rubio, “Atoms and Molecules in Cavities, from Weak to Strong Coupling in Quantum-Electrodynamics (QED) Chemistry,” *Proc. Natl. Acad. Sci.* **114**, 3026–3034 (2017).
- <sup>27</sup>R. R. Riso, T. S. Haugland, E. Ronca, and H. Koch, “Molecular Orbital Theory in Cavity QED Environments,” *Nat. Commun.* **13**, 1368 (2022).
- <sup>28</sup>C. Schäfer, J. Flick, E. Ronca, P. Narang, and A. Rubio, “Shining Light on the Microscopic Resonant Mechanism Responsible for Cavity-Mediated Chemical Reactivity,” *Nat. Commun.* **13**, 7817 (2022).
- <sup>29</sup>J. Bonini and J. Flick, “Ab Initio Linear-Response Approach to Vibro-polaritons in the Cavity Born-Oppenheimer Approximation,” *J. Chem. Theory Comput.* **18**, 2764–2773 (2021).
- <sup>30</sup>J. Yang, Q. Ou, Z. Pei, H. Wang, B. Weng, Z. Shuai, K. Mullen, and Y. Shao, “Quantum-Electrodynamical Time-Dependent Density Functional Theory within Gaussian Atomic Basis,” *J. Chem. Phys.* **155**, 064107 (2021).
- <sup>31</sup>B. Rosenzweig, N. M. Hoffmann, L. Lacombe, and N. T. Maitra, “Analysis of the Classical Trajectory Treatment of Photon Dynamics for Polaritonic Phenomena,” *J. Chem. Phys.* **156**, 054101 (2022).
- <sup>32</sup>J. F. Triana, F. J. Hernández, and F. Herrera, “The Shape of the Electric Dipole Function Determines the Sub-picosecond Dynamics of Anharmonic Vibrational Polaritons,” *J. Chem. Phys.* **152**, 234111 (2020).
- <sup>33</sup>T. E. Li, J. E. Subotnik, and A. Nitzan, “Cavity Molecular Dynamics Simulations of Liquid Water under Vibrational Ultrastrong Coupling,” *Proc. Natl. Acad. Sci.* **117**, 18324–18331 (2020).
- <sup>34</sup>H. Deng, H. Haug, and Y. Yamamoto, “Exciton-Polariton Bose-Einstein Condensation,” *Rev. Mod. Phys.* **82**, 1489–1537 (2010).
- <sup>35</sup>J. Keeling and S. Kéna-Cohen, “Bose-Einstein Condensation of Exciton-Polaritons in Organic Microcavities,” *Annu. Rev. Phys. Chem.* **71**, 435–459 (2020).
- <sup>36</sup>H. L. Luk, J. Feist, J. J. Toppari, and G. Groenhof, “Multiscale Molecular Dynamics Simulations of Polaritonic Chemistry,” *J. Chem. Theory Comput.* **13**, 4324–4335 (2017).
- <sup>37</sup>R. H. Tichauer, J. Feist, and G. Groenhof, “Multi-scale Dynamics Simulations of Molecular Polaritons: The Effect of Multiple Cavity Modes on Polariton Relaxation,” *J. Chem. Phys.* **154**, 104112 (2021).
- <sup>38</sup>I. Sokolovskii, R. H. Tichauer, D. Morozov, J. Feist, and G. Groenhof, “Enhanced Excitation Energy Transfer under Strong Light-Matter Coupling: Insights from Multi-Scale Molecular Dynamics Simulations,” arXiv (2022), arXiv:2209.07309.
- <sup>39</sup>M. Sukharev, J. Subotnik, and A. Nitzan, “Dissociation Slowdown by Collective Optical Response Under Strong Coupling Conditions,” *J. Chem. Phys.* **158** (2023), 10.1063/5.0133972/2868724.
- <sup>40</sup>E. Suyabatmaz and R. F. Ribeiro, “Vibrational Polariton Transport in Disordered Media,” *J. Chem. Phys.* **159** (2023), 10.1063/5.0156008/2902632.
- <sup>41</sup>W. Ying, M. A. D. Taylor, and P. Huo, “Microscopic Theory of Vibrational Polariton Chemistry,” (2023), arXiv:2305.05005.
- <sup>42</sup>T. E. Li, A. Nitzan, S. Hammes-Schiffer, and J. E. Subotnik, “Quantum Simulations of Vibrational Strong Coupling via Path Integrals,” *J. Phys. Chem. Lett.* **13**, 3890–3895 (2022).
- <sup>43</sup>A. Z. Lieberherr, S. T. Furniss, J. E. Lawrence, and D. E. Manolopoulos, “Vibrational Strong Coupling in Liquid Water from Cavity Molecular Dynamics,” *J. Chem. Phys.* **158**, 234106 (2023).
- <sup>44</sup>T. E. Li, A. Nitzan, and J. E. Subotnik, “Polariton Relaxation under Vibrational Strong Coupling: Comparing Cavity Molecular Dynamics Simulations against Fermi’s Golden Rule Rate,” *J. Chem. Phys.* **156**, 134106 (2022).
- <sup>45</sup>T. E. Li, A. Nitzan, and J. E. Subotnik, “Cavity Molecular Dynamics Simulations of Vibrational Polariton-enhanced Molecular Nonlinear Absorption,” *J. Chem. Phys.* **154**, 094124 (2021).
- <sup>46</sup>B. Xiang and W. Xiong, “Molecular Vibrational Polariton: Its Dynamics and Potentials in Novel Chemistry and Quantum Technology,” *J. Chem. Phys.* **155**, 050901 (2021).
- <sup>47</sup>T. E. Li, A. Nitzan, and J. E. Subotnik, “Energy-Efficient Pathway for Selectively Exciting Solute Molecules to High Vibrational States via Solvent Vibration-Polariton Pumping,” *Nat. Commun.* **13**, 4203 (2022).
- <sup>48</sup>T. E. Li and S. Hammes-Schiffer, “QM/MM Modeling of Vibrational Polariton Induced Energy Transfer and Chemical Dynamics,” *J. Am. Chem. Soc.* **145**, 377–384 (2023).
- <sup>49</sup>C. Cohen-Tannoudji, J. Dupont-Roc, and G. Grynberg, *Photons and Atoms: Introduction to Quantum Electrodynamics* (Wiley, New York, 1997) pp. 280–295.
- <sup>50</sup>To derive Eq. (11) from Eq. (3), we have used the following identities:  $-\frac{1}{\epsilon_0} \int d\mathbf{r} \mathbf{D}_\perp(\mathbf{r}) \cdot \hat{\mathcal{P}}_\perp(\mathbf{r}) = -\frac{1}{\epsilon_0} \int d\mathbf{r} \mathbf{D}_\perp(\mathbf{r}) \cdot \hat{\mathcal{P}}(\mathbf{r}')$ , and  $\frac{1}{2\epsilon_0} \int d\mathbf{r} |\hat{\mathcal{P}}_\perp(\mathbf{r})|^2 = \frac{1}{2\epsilon_0} \int d\mathbf{r} \int d\mathbf{r}' \hat{\mathcal{P}}(\mathbf{r}) \hat{\delta}_\perp(\mathbf{r} - \mathbf{r}') \hat{\mathcal{P}}(\mathbf{r}')$ .
- <sup>51</sup>J. Flick, H. Appel, M. Ruggenthaler, and A. Rubio, “Cavity Born-Oppenheimer Approximation for Correlated Electron-Nuclear-Photon Systems,” *J. Chem. Theory Comput.* **13**, 1616–1625 (2017).
- <sup>52</sup>W. P. Schleich, *Quantum Optics in Phase Space* (Wiley, 2001) p. 232.
- <sup>53</sup>T. E. Li, A. Nitzan, and J. E. Subotnik, “Collective Vibrational Strong Coupling Effects on Molecular Vibrational Relaxation and Energy Transfer: Numerical Insights via Cavity Molecular Dynamics Simulations,” *Angew. Chemie Int. Ed.* **60**, 15533–15540 (2021).
- <sup>54</sup>T. E. Markland and M. Ceriotti, “Nuclear Quantum Effects Enter the Mainstream,” *Nat. Rev. Chem.* **2**, 0109 (2018).
- <sup>55</sup>V. Kapil, M. Rossi, O. Marsalek, R. Petraglia, Y. Litman, T. Spura, B. Cheng, A. Cuzzocrea, R. H. Meißner, D. M. Wilkins, B. A. Helfrecht, P. Juda, S. P. Bienvenue, W. Fang, J. Kessler, I. Poltavsky, S. Vandenbrande, J. Wieme, C. Corminboeuf, T. D. Kühne, D. E. Manolopoulos, T. E. Markland, J. O. Richardson, A. Tkatchenko, G. A. Tribello, V. Van Speybroeck, and M. Ceriotti, “I-PI 2.0: A Universal Force Engine for Advanced Molecular Simulations,” *Comput. Phys. Commun.* **236**, 214–223 (2019).
- <sup>56</sup>M. Rossi, M. Ceriotti, and D. E. Manolopoulos, “How to Remove the Spurious Resonances from Ring Polymer Molecular Dynamics,” *J. Chem. Phys.* **140**, 234116 (2014).
- <sup>57</sup>D. A. McQuarrie, *Statistical Mechanics* (Harper-Collins Publishers, New York, 1976).
- <sup>58</sup>M.-P. Gaigeot and M. Sprik, “Ab Initio Molecular Dynamics Computation of the Infrared Spectrum of Aqueous Uracil,” *J.*

- Phys. Chem. B **107**, 10344–10358 (2003).
- <sup>59</sup>S. Habershon, G. S. Fanourgakis, and D. E. Manolopoulos, “Comparison of Path Integral Molecular Dynamics Methods for the Infrared Absorption Spectrum of Liquid Water,” *J. Chem. Phys.* **129**, 074501 (2008).
- <sup>60</sup>A. Nitzan, *Chemical Dynamics in Condensed Phases: Relaxation, Transfer and Reactions in Condensed Molecular Systems* (Oxford University Press, New York, 2006).
- <sup>61</sup>V. M. Agranovich, M. Litinskaia, and D. G. Lidzey, “Cavity Polaritons in Microcavities Containing Disordered Organic Semiconductors,” *Phys. Rev. B* **67**, 085311 (2003).
- <sup>62</sup>S. Pannir-Sivajothi, J. A. Campos-Gonzalez-Angulo, L. A. Martínez-Martínez, S. Sinha, and J. Yuen-Zhou, “Driving chemical reactions with polariton condensates,” *Nat. Commun.* **13**, 1645 (2022).